CHARACTERIZATION OF TRAJECTORIES OF MAGNETICALLY
ACTUATED MICROSWIMMERS WITH HELICAL TAILS
IN CIRCULAR CHANNELS

by

HAKAN OSMAN ÇALDAĞ

Submitted to the Graduate School of Engineering and Natural Sciences
in partial fulfillment of
the requirements for the degree of
Master of Science

Sabanci University

August 2016

CHARACTERIZATION OF TRAJECTORIES OF MAGNETICALLY ACTUATED MICRO SWIMMERS WITH HELICAL TAILS IN CIRCULAR CHANNELS

APPROVED BY:

Prof. Dr. Serhat Yeşilyurt
(Thesis Supervisor)
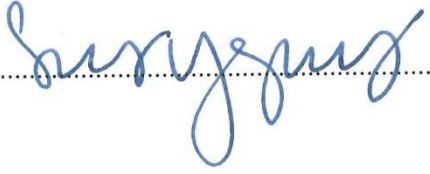
Asst. Prof. Dr. Meltem Elitaş

Prof. Dr. Ata Muğan

DATE OF APPROVAL: ......02./08./2016...........

ABSTRACT

CHARACTERIZATION OF TRAJECTORIES OF MAGNETICALLY
ACTUATED MICROSWIMMERS WITH HELICAL TAILS
IN CIRCULAR CHANNELS

HAKAN OSMAN ÇALDAĞ

M.Sc. Thesis, August 2016

Supervisor: Professor Serhat Yeşilyurt

Keywords: Microswimmer, Low Reynolds Number Swimming, Computational
Fluid Dynamics, Motion in Circular Confinement, Motion Control

Micro swimming robots can pave the way for a vast range of applications such as targeted drug delivery, minimally invasive surgery and they can also be used as agents in microsystems. Though it is now possible to manufacture nano-scale swimming structures, motion of these swimmers is yet to be understood in full. Understanding microswimmer motion is crucial in controlling the swimmers. The aim of this thesis is to present an overall picture of trajectory of a microswimmer with a magnetic head and helical tail inside circular channels filled with glycerol. Millimeter long swimmers are produced with 3D printing technology. The swimmers are propelled by a rotating magnetic field achieved by giving alternating current to Helmholtz coil pairs. Effects of confinement, tail length and fluid flow on swimmer trajectory, orientation and propulsion and lateral velocities are reported. It is observed that backward and forward motion of a swimmer result in different trajectories. Amount of confinement affects the way the swimmer follows this trajectory. Fluid flow affects swimming depending on the ratio of tail length to channel size. Direction of fluid flow alters radius of the trajectory. The magnetic field is modulated in order to control the swimmer's direction of motion. Modulated field can be used to make the swimmer follow a straight trajectory close to the center of the channel. Experimental studies are validated with two computational fluid dynamics (CFD) models; one giving out the average swimming behavior and the other giving full trajectory in a time-dependent fashion.

ÖZET

MANYETİK ŞEKİLDE TAHRİK EDİLEN SARMAL KUYRUKLU MİKROYÜZÜCÜLERİN SİLİNDİRİK KANALLARDAKİ GEZİNGELERİNİN KARAKTERİZASYONU

HAKAN OSMAN ÇALDAĞ

Yüksek Lisans Tezi, Ağustos 2016

Tez Danışmanı: Profesör Serhat Yeşilyurt

Anahtar Kelimeler: Mikroyüzücü, Düşük Reynolds Sayısında Yüzme, Hesaplamalı Akışkanlar Dinamiği, Silindirik Kanallarda Hareket, Hareket Kontrolü

Mikroyüzücü robotlar hedef dokuya ilaç teslimi, düşük zararlı cerrahi ameliyatlar ve mikro sistemlere müdahale gibi geniş bir uygulama yelpazesinin önünü açabilirler. Her ne kadar artık nano ölçekte yüzen yapılar üretmek mümkün olsa da, bu yüzücülerin hareketi henüz tam olarak anlaşılamamıştır. Mikroyüzücü hareketinin anlaşılması bu yüzücüleri kontrol edebilmede büyük öneme sahiptir. Bu tezin amacı manyetik bir kafa ve sarmal bir kuyruğa sahip olan bir mikroyüzücünün gliserin dolu silindirik kanallardaki gezingesi hakkında etraflıca bir fikir vermektir. Milimetre ölçeğinde yüzücüler üç boyutlu yazıcı teknolojisi kullanılarak üretilmiştir. Bu yüzücüler alternatif akım verilen Helmholtz bobini çiftleriyle oluşturulan döner manyetik alanla ileri doğru sürülmektedir. Kanal genişliği, kuyruk uzunluğu ve sıvı akışının yüzücü gezingesi, yönelimi ve tahrik ve yanal hızına etkisi bildirilmektedir. Bir yüzücünün ileri ve geri hareketinin farklı gezingelere yol açtığı gözlemlenmiştir. Kanal genişliği yüzücünün bu gezingeleri takip şeklini etkilemektedir. Sıvı akışı, kuyruk uzunluğunun kanal genişliğine oranına bağlı olarak yüzüşü etkilemektedir. Sıvı akışının yönü gezingenin yarıçapına etki etmektedir. Yüzücünün hareket yönünü kontrol etmek için manyetik alan değiştirilmiştir. Değiştirilmiş manyetik alan yüzücünün kanal merkezine yakın düz bir gezinge izlemesinde kullanılmıştır. Deneysel çalışmalar iki adet hesaplamalı akışkanlar dinamiği modeliyle doğrulanmıştır. Bu modellerden biri yüzücünün ortalama davranışını gösterirken diğeri yüzücünün tüm gezingesini zamana bağlı bir şekilde ortaya çıkarmaktadır.

ACKNOWLEDGEMENTS

TABLE OF CONTENTS

LIST OF FIGURES

LIST OF TABLES

LIST OF SYMBOLS

β Dimensionless radial position of the swimmer

B Magnetic field magnitude

B_0 Nondimensional magnetic torque

B_{sw} Amplitude of helical wave of the tail of the swimmer

B_x x- component of magnetic field vector

B_y y- component of magnetic field vector

B_z z- component of magnetic field vector

Δt Time step

Δw Threshold distance to channel wall to avoid collision

D   Channel diameter (compact notation)

D_{ch} Channel diameter

D_{head} Diameter of swimmer head

D_{tail} Diameter of the filament tail

ε Very small value to avoid division by zero

$\mathbf{e_i}$ Unit vectors of local coordinate frame on swimmer head, for i = 1, 2, 3

$\mathbf{F}_{f_j}$ Force of the fluid on the swimmer for j = 1, 2, 3

F_r Wall reaction force

f Rotation rate

I_i Amount of current passing through Helmholtz coils for i = 1, 2, 3

I_j Amplitude of the current passing through Helmholtz coils for j = A, B, C

λ Wavelength of helical wave of the swimmer tail

L	Swimmer length (compact notation)
L_o	Overall length of the swimmer
L_{scale}	Length scale
L_{tail}	Swimmer tail length
L_{head}	Swimmer head length
μ	Viscosity of fluid the swimmer is placed in
μ_0	Permeability of free space
M	Magnetic moment
m	Magnetization vector
m_m	Magnetization of swimmer magnet
m_0	Magnitude of magnetization vector
m_x	x- component of unit magnetization vector of permanent magnet
m_y	y- component of unit magnetization vector of permanent magnet
m_z	z- component of unit magnetization vector of permanent magnet
N	Number of turns in a Helmholtz coil
n	Time step
n_{ref}	Refractive index
n_i	Components of normal of small surface dS for i = 1, 2, 3
Q	Flow rate (compact notation)
θ	Orientation of the swimmer on y-z plane
θ_r	Orientation of swimmer in cylindrical coordinates, in r- direction
θ_θ	Orientation of swimmer in cylindrical coordinates, in θ- direction
θ_{xy}	The angle the fit line makes with +x axis in x-y plane
θ_{xy}	The angle the fit line makes with +x axis in x-z plane
ρ	Nondimensional density of fluid the swimmer is placed in
ρ_{head}	Density of swimmer head

ρ_{tail}	Density of swimmer tail
p	Nondimensional pressure
p_s	Slope of the line fit to the extracted points within swimmer region in image
R	Rotation matrix that rotates the swimmer from its neutral orientation to desired one
R_{ch}	Radius of the channel
R_{he}	Radius of Helmholtz coil
R_{head}	Radius of swimmer head
R_{local}	Rotation matrix that transforms global coordinates to local coordinates defined on swimmer head
$\mathbf{r}$	Position vector of the swimmer in Cartesian coordinates
$\mathbf{r^*}$	New unit vector of radial component of cylindrical coordinate system
r	Radial position of the swimmer
r_{mean}	Mean radial position of the swimmer in an experiment
r_{sw}	Radial position of the swimmer
Re	Reynolds number
σ_{ij}	Components of Cauchy stress tensor field for i = 1, 2, 3 and j = 1, 2, 3
σ_r	Radial stress on the swimmer
σ_{wall}	Wall stress on the swimmer
S	Surface of the swimmer
$\boldsymbol{\tau_f}$	Fluid torque on swimmer
$\boldsymbol{\tau_g}$	Gravitational torque on swimmer
$\boldsymbol{\tau_{g,head}}$	Gravitational torque on swimmer due to head weight
$\boldsymbol{\tau_{g,tail}}$	Gravitational torque on swimmer due to tail weight
$\boldsymbol{\tau_m}$	Magnetic torque on swimmer
t	Time in seconds
t_{scale}	Time scale

1

INTRODUCTION

Inspired by natural swimmers such as bacteria, artificial microswimmers hold great potential in becoming controllable agents of micro world. *In vivo* applications such as targeted drug delivery, minimally invasive surgery and *ex vivo* applications such as cargo delivery, micro system manipulation show how versatile they can be. The developments in micro fabrication methods have allowed production of micron-scale artificial swimmers with helical tails [1, 2]. Though the production capabilities have improved, controllability of these agents remains as a great concern considering that the application areas of these swimmers require high controllability. There are many parameters that change the swimming behavior of a swimmer such as swimmer geometry, confinement, fluid in which the swimmer is placed and fluid flow. The effects of variation of these parameters have to be understood very well in order to establish the fundamentals in controlling the swimmers.

Swimmers consisting of a helical tail and a head structure are widely adopted in the literature, inspired by microorganisms that propel with their flagella. External actuation methods such as magnetic field are used since self-actuation methods are costly [3]. If the swimmers are in a visible environment, they can be tracked visually for control while invisibility necessitates more complicated tracking methods such as ultrasound, magnetic resonance imaging (MRI) or computer tomography (CT) [3].

The objective of this thesis is to establish the fundamentals of trajectories of microswimmers with helical tails. The swimmers are tested in circular channels so as for observations to hold validity in vascular system. Geometry of swimmer tail, confinement and fluid flow rate are varied to characterize swimmer motion. Geometrical variation allows for design optimization of the tail while confinement is observed in living

organisms to change swimming trajectories so characterization with respect to confinement is important as well. Understanding the effect of fluid flow on trajectories is necessary especially in the case of vascular applications. The experimental studies are complemented with two different computational fluid dynamics (CFD) models to both validate our observations and to further develop computational microswimmer studies.

With the findings of this thesis, fundamentals of trajectories of helical microswimmers in circular channels will be laid out which would be crucial in controllability of the swimmers. Not only the swimmer motion can be controlled, but also swimmer motion can be planned or predicted ahead of time which would be beneficial for *in vivo* applications where accurately and timely tracking may not be possible.

1.1. Background

1.1.1. Experimental Studies

Before giving the background on the work field, it is important to explain the swimming environment of microswimmers, which differ greatly from human scale swimming environments. The swimming environment microswimmers swim in most often have a Reynolds number on the order of $10^{-5} \sim 10^{-2}$. This range of Reynolds numbers mean that viscous forces dominate inertial forces such that inertia of a microswimmer is negligible. According to the scallop theorem, swimming at low Reynolds numbers can't be achieved by reciprocal motion [4]. Instead, the motion should be such that it's not reversible in time. An example to such a movement type is the motion of *Escheria coli* bacterium which has a rotating bundle of helical flagella to swim. One can't shake off its environment in a low Reynolds number environment; the environment falls back the swimmer gradually as it keeps moving on [4]. Other than low Reynolds number swimming, since microswimmers are at a smaller scale, Brownian motion, random movement of microscopic objects in fluid caused by constant thermal agitation, has to be taken into account as well [5].

1.1.1.1. Work on living organisms

Microorganisms have several different methods to move in an aqueous environment: While some organisms move by deforming their bodies in time (amoeboid motion), some organisms have special segments for moving in liquid such as cilia in paramecium or helical flagellar filaments in various types of bacteria [6, 7]. Helical flagellar filaments have received significant attention as bacteria with flagella constitute a significant portion of bacteria that exhibit active motion [7]. These filaments are generally a few to ten μm in length, 40 nm in diameter and made of a protein called flagellin [7]. The filaments are attached to the cell body through a hook. Rotation of the hook is achieved by flux of ions such as H^+ or Na^+. This rotary motor works at constant torque in counterclockwise direction for a wide range of frequencies while it decreases linearly with increasing frequency in the clockwise direction [7].

Bacteria with multiple flagella rotate their flagella in both of these directions; winding and unwinding the tail periodically: This is called run-and-tumble motion [8]. Run-and-tumble is observed to allow the bacterium to change its direction of motion during tumbling stage [8]. Single flagellated bacteria can't change swimming direction by themselves as they can't tumble [5]. To keep swimming force and torque-free, swimmer body and flagella rotate in opposite directions [5].

Depending on the rotation direction of flagella, microswimmer motion is classified under two main categories: One of them is called pusher mode in which the propelling apparatus pushes the swimmer body and the other one is called puller mode in which the propelling apparatus pulls the swimmer body. For a right-handed flagellum, a clockwise rotation (viewed from outside of the cell) means pushing and rotation in counterclockwise direction means pulling motion [9]. These two types of motion lead to propulsion in opposite directions. Interestingly, despite similar propulsion velocities in both modes, it was observed that *Caulobacter crescentus* bacteria rotate their flagella two times faster in puller mode [9].

Precession occurs in pusher mode swimming, causing the bacteria to trace out a helical trajectory while in the puller mode precession is much lower [9]. Another study on *Caulobacter crescentus* reports that motor torque in puller mode is larger than it is in

pusher mode, hence explaining similar propulsion despite different rotation rates [10]. So, the thrust developed in these two modes is independent of direction of motion [10].

Swimming speed increases linearly with rotation rate but saturates if the rotation rate increases further [11]. Observations on *Vibrio Alginolyticus* bacteria reveal that the ratio of swimming speed to rotation rate is independent of temperature dependent parameters such as viscosity and density [11].

Alongside understanding fundamentals of bacteria motion, there has been extensive research on bacteria near surfaces and under confinement. Bacteria accumulation at surfaces is a common observation and its dynamics are studied extensively in order to understand biofilm formation. When *Escheria coli* are placed between two parallel plates, they are observed to accumulate nearby the plates, which is explained by hydrodynamic trapping [12]. Nearby a surface, the bacteria swim in circles due to their rotation [13]. Observations reveal that the bacteria follow a helical path since their flagella pushes them off-axis relative to their bodies [14]. Lauga et al. [15] find that radius of curvature of the circular trajectory increases with the body length. Though bacteria tend to accumulate near surfaces, they rarely hit the surface [8].

Understanding swimmer motion in channels is important as well since it would contribute to applications *in vivo* and *ex vivo* such as vascular system and lab-on-a-chip devices. Single-cell motility parameters in micro fabricated planar channels remain nearly constant even at the channels at the size of the bacteria, *ca* 2 μm [16]. However, the velocity of the organism is reduced by 25% in 2-μm channels while the velocity is increased by 10% in 3-μm channels in comparison to the free swimming velocity [16]. In narrow tubes, the bacteria move in one dimension only [17]. The increase in drift velocities of bacteria moving through 10-μm channel compared to 50-μm channel indicates that alignment of cell trajectory with the channel's axis increases the velocity [17]. Another study reports that *E. coli* prefer to swim on right hand side in channels [18]. For example, bacteria swim close to porous agar surface at the bottom but swim away from solid PDMS surface, resulting in a preference towards right-hand side [18]. The same study also finds that short-range molecular interactions such as van der Waals forces are not significant in preferential cell motion; these forces are significant when the distance of a bacterium to a surface is less than 10 nm [16, 18]. Confinement is increased to an extreme value in one study such that channel width is lower than bacteria width

[19]. *E. coli* is motile in channels down until a channel width of 1.3 times the size of the bacterium [19]. This lower limit for motility is explained by several factors such as hydrodynamic drag, adhesion forces and geometric constraints to flagellar motion [19]. Strikingly, at even smaller channels, the bacterial dispersal is driven by growth and reproduction [19].

1.1.1.2. Work on artificial structures

With the developments in micro and nanofabrication methods, it has become possible to produce artificial microswimmers. In-channel experiments of cm-scale microswimmers date back to 1996 [20]. One of the very first attempts at producing a micro-scale artificial structure is by Dreyfus et al. [21] in which the swimmer consists of a linear chain of colloidal magnetic particles (coated with streptavidin) linked by DNA molecules, attached to a red blood cell. The cell is propelled by a time varying magnetic field causing undulatory tail motion alongside an additional static magnetic field to keep the swimmer straight [21]. A similar approach in incorporating living organisms is the placement of magnetite particles (called magnetosomes) into bacteria [3]. These bacteria are known as magnetotactic bacteria. The magnetic particles act like a magnetic compass needle and allow for navigation of bacterium. While this method reduces cost and eases reproducibility, there are problems such as immune system response and cytotoxicity level [3].

As fabrication techniques improve, completely artificial structures could be manufactured: One study reports a self-scrolling technique to obtain a helical magnetic tail with a diameter of 2.8 μm while Ghosh and Fischer employ glancing angle vapor deposition method to fabricate micron long, 200-300 nm wide swimmers made of SiO_2 with a thin ferromagnetic coating [1, 22]. In another study, 3D laser printing and physical vapor deposition are employed to produce 35 μm long, 6 μm diameter swimmers [2].

Propulsion methods other than magnetic field are employed as well: In a recent study, cylindrical microswimmers made of liquid-crystal elastomers that exhibit response to light are produced [23]. By exposing the swimmer to structured monochromatic light, these swimmers are able to swim peristaltically like a worm [23]. Acemoglu and Yesilyurt [24] produce millimeter scale helical microswimmers by 3D printing and attach a radially

polarized neodymium magnet to its head to actuate the swimmer with a rotating magnetic field. The reason magnetic field is preferred is due to its *in vivo* applicability. However, *in vivo* applicability remains to be a challenge as the swimmers themselves are not biocompatible. Another problem in *in vivo* applicability is the issue of imaging: While there are many alternatives such as ultrasound, PET, X-ray, CT and MRI; they either lack proper resolution or timeliness for proper feedback and control [3]. Specialized methods such as Magnetic Signature Selective Excitation Tracking have been developed to overcome the time delay in MR imaging but the system has difficulties in tracking beads smaller than 1.5 mm, which is large if vascular system is considered [3]. Abbott et al. [25] compare various magnetic actuation mechanisms and conclude that microswimmers with helical tails and flexible flagella perform better than swimmers actuated by magnetic field gradient and swimmers whose head are oscillated. Magnetic field gradients are risky for human health so they can't be utilized to full extent [3].

There are several important observations on swimming dynamics of microswimmers in these experiments. Firstly, swimming velocity is found to be proportional to the rotation rate of the swimmer up until a step-out frequency where the viscous torque dominates the magnetic torque and the swimmer is not able to keep up with the rotating magnetic field anymore [1]. Viscosity and strength of the magnetic field affect step-out rotation rate but they do not enhance or hinder propulsion. Swimmers with larger diameters are found to swim faster and it is concluded that the velocity depends on the characteristic length of the helix [2]. In a macro scale study, a helical swimmer is placed inside a viscoelastic fluid to account for low Reynolds number swimming in micro scale [26]. A critical Deborah number of 1, meaning that rotation rate of the swimmer is equal to relaxation rate of the viscoelastic fluid, is found to enhance the swimming velocity most [26]. Acemoglu and Yesilyurt [24] report that puller mode swimming is more stable than pusher mode swimming. They also demonstrate that confinement improves the stability of swimmer trajectories in circular channels [24]. Another observation from the same study is that the step-out is suppressed when the swimming is in flow direction. [24].

1.1.2. Theoretical Understanding and Computational Studies

The basic understanding of microswimmer motion comes from two theories. In resistive force theory, hydrodynamic force acting on a helix moving through the field per unit length is locally proportional in an anisotropic fashion to local body velocity and the coefficient of proportionality is drag coefficient [27, 28]. However, Lighthill [30] showed that this assumption is invalid as the viscous effects dominate and produce long-range hydrodynamic interactions [28]. Comparing the accuracy of resistive force theory and Lighthill's slender body theory, Johnson and Brokaw find slender body theory to be more accurate but favor resistive force theory since the amount of increase in accuracy does not justify the extra computational cost [28]. There are studies that use different models as well. Felderhof [29] uses perturbation theory to second order to model an infinitely long swimmer moving by surface deformation with various swimming types such as axisymmetric, undulatory and helical motion. He finds that confinement increases efficiency of helical swimmer in between parallel walls [29]. Alongside these theoretical models, developments in computational fluid dynamics (CFD) and boundary element method (BEM) led to solution of Stokes equations [31]. There is a study based on resistive force theory focusing on the transition from wobbling to swimming for magnetically actuated swimmers where the authors relate wobbling with Mason number (Ma), defined as the ratio of hydrodynamic torque to magnetic torque [27]. Low Ma number means wobbling while higher Ma number means there is no wobbling. For all Ma numbers, wobbling angle (which is zero if there is no wobbling) reaches a steady value under a given configuration [27]. Swimmers with larger number of wavelengths and smaller number of helix angles are found to start directed swimming quicker [27]. Elimination of wobbling is important as wobbling decreases the energy efficiency and lost work will be dissipated as heat which is concerning for a biological environment [27].

Shum et al. [32] optimize the power and torque generation of microswimmers by changing geometric parameters using a BEM model. They find that short swimmers with small wavelengths should be chosen for torque efficiency while for power efficiency longer swimmers with higher wavelengths should be preferred [32]. With such results, it turns out that power efficient swimmers are boundary accumulators while torque efficient swimmers are boundary escapers [32]. It is also reported that height of accumulation decreases with decreasing aspect ratio, with spherical swimmers tending to descend into

boundary [32]. Another work by Shum and Gaffney [33] uses BEM again to model swimming around the corner of a rectangular channel. They treat a bundle of flagella as a single flagellum as this assumption gives results close to experimental observations and computational cost is reduced [33]. They propose circular channels instead of rectangular ones to prevent colonization at corners since even the boundary escapers remain trapped at the corners of the channel [33]. Goto and Masuda [34] conduct experiments with *Vibrio Alginolyticus* and also build a BEM model to confirm that swimming velocity is proportional to rotation rate and torque generation is on the order of pN·m. Another study on *Vibrio Alginolyticus* reports that swimming velocity is proportional to rotation rate but it saturates if rotation rate is increased further, similar to step-out observed for artificial swimmers [11]. The authors model the torque characteristics in two types in which the torque is either constant or decreasing with increased rotation [11]. Constant torque model is valid for low rotation rates while decreasing torque model is valid at high rotation rates which explains the saturation of swimming velocity [11].

Zöttl and Stark [35] solve non-linear dynamics of a very small spherical swimmer in cylindrical Poiseuille flow in three dimensions using dipole approximation. They find solutions in which the swimmer exhibits swinging or tumbling motion. The distinction of swinging motion is that the swimmer passes through the channel centerline periodically whereas in tumbling motion it can't pass [35]. Pushers tend to go towards channel wall, following an oscillatory trajectory around the centerline while pullers follow a stable trajectory around the centerline [35]. Whether the swimmer exhibits swinging or tumbling motion depends on flow rate; that is, the swimmer can't do swinging motion if there's too much flow [35]. In Zöttl and Stark's [36] another study, it is reported that the distinction of non-spherical swimmers is that not only the flow vorticity contributes to swimmer's angular velocity but also strain rates have to be taken in consideration [36]. Strain rates are why elongated swimmers rotate slower when oriented in flow direction [36]. Aspect ratio of the channel determines the frequency of periodic motion [36]. Swinging and tumbling are observed at all cases [36]. Graaf and Mathjissen [37] calculate the higher order hydrodynamic interactions of a rod-shaped swimmer using a combination of lattice-Boltzmann simulations and far-field calculations. They find that quadrupole moments are the cause of oscillatory trajectories [37]. Continual rotation away from the wall establishes these oscillations [37]. Consideration of lower order interactions only results in attraction to boundary [37]. Quadrupolar moments have to be included to observe

oscillations about the center [37]. Change of aspect ratio only leads to a second-order correction as hydrodynamic moments dominate the dynamics of swimming [37]. Chacón [38] studies the motion of a spherical microswimmer in a cylindrical Poiseuille flow to discover that the regularity of the motion of a swimmer depends on small finite periodic oscillations that vary with the position and the orientation of the swimmer in the channel and also efficient upstream (downstream) swimming takes place at (away from) the center. Zhu et al. [39] present the results of a BEM model of a spherical squirmer in a circular tube with a diameter on the order of swimmer size. When the swimmer is swimming parallel to channel axis, locomotion speed is always reduced for swimmers with tangential deformation while it is increased in the case of normal deformation [39]. The squirmers with no force dipoles in the far field generally follow helical trajectories [39]. Maximum velocity is achieved when the swimmer is close to channel wall [39]. Pushers end up crashing at the walls while pullers with a weak dipole follow the channel centerline and pullers with a strong dipole follow a stable trajectory around the wall [39]. Since pullers don't crash into walls, they can take advantage of near-wall hydrodynamics to enhance their swimming velocity [39]. For pushers to take advantage of near-wall interactions, they should go through a combination of normal and tangential deformation [39].

While these studies are on bacteria or theoretic artificial structures, there are computational studies on real artificial swimmers as well: Keaveny et al. [40] model the swimmer in Dreyfus et al. [21] in the computational domain in three dimensions. Temel and Yesilyurt [41] solve steady Stokes equations and demonstrate effects of geometric parameters on velocities of microswimmers composed of a magnetic head and a helical tail. Forward velocities differ depending on swimmer positioning as squeezed fluid between channel boundaries and swimmer is forced to move in opposite directions so swimming in center and near the wall differ [41]. Forces in directions other than channel's axis direction are nearly zero when the swimmer is in center [41]. Acemoglu and Yesilyurt [24] report the effects of flow rate, showing that the linear relationship between swimmer rotation rate and swimming velocity is disturbed. They fit experimental observations to two sets of computational data where the swimmer is either at the center of the channel or close to the walls [24]. In puller mode, the swimmer follows the computational results at the center closely while in the pusher mode the experimental results follow the computational results for near-wall swimming [24]. However, the

tendency of experimental results to follow the results of simulations at the center or near-wall depends on confinement [24].

1.1.3. Efforts on Microswimmer Control

There are several studies on controlling both living and artificial microswimmers. Attraction of bacteria towards surfaces is seen as an opportunity in controlling bacteria motion and distribution. One study examines the behavior of bacteria near funnel-shaped openings and it is found that these walls can be used to form well-defined bacteria patterns [13]. Ghosh and Fischer [22] are able to control an artificial swimmer in micrometer scale by applying a small magnetic field. Zhang et al. [42] use a third pair of Helmholtz coils (in addition to two pairs to rotate helical swimmer) to steer a microswimmer as desired. The modulation of the field in such a fashion can lead to two possible rotations depending on relative swimmer position but as long as the misalignment of the magnetic field (compared to perfectly aligned magnetic field) is less than 45° compared to the desired rotation axis, the swimmer chooses the desired axis [42]. Another study models bacteria swimming with multiple flagella and applies control to make the swimmer track a 3D path, reporting that the swimmer can perform 3D maneuvers if the swimmer has at least 3 flagella [43]. Oulmas et. al. [44] take 3D path following problem one step further and build a control algorithm that works on visual feedback by controlling the magnetic field generated by three pairs of Helmholtz coils, controlling linear and angular velocities. The algorithm is reported to work with real-life, millimeter-scale microswimmers in a glycerol-filled environment [44].

1.2. Novelties of the Thesis

The aim of this thesis is to provide the reader with an understanding of swimming behavior of a magnetically actuated artificial microswimmer with helical tail in a circular channel by showing the effects of variation in helical tail length, channel size and fluid flow. The experimental observations are supported by steady-state and time-dependent CFD models which solve Stokes equations.

The swimmers are produced using 3D printing technology. Permanent magnets are placed on the head section of the swimmers which acts as a holder. The swimmers are rotated by applying out-of-phase currents to two pairs of Helmholtz coils which generate a rotating magnetic field. The swimmer is placed in a circular tube filled with glycerol (to have low Reynolds number) placed in the center of Helmholtz coil pairs such that magnetization vector of the swimmer head is perpendicular to the rotating magnetic field. Experiments with swimmers of four different tail lengths are conducted in two differently sized channels under four different flow rates (one of which is the case of no flow). 3D trajectory, orientation and swimming and lateral velocities of the swimmer are extracted from experiment videos with image processing tools. The algorithm is suitable for any kind of swimmer as long as its color contrasts with the background.

Control efforts consist of using a third pair of Helmholtz coils that modulates the rotating magnetic field created by two Helmholtz coil pairs. The swimmer is made to move in four main directions (i.e., up, down, left, right). Modulated fields are alternated to achieve more complicated motion. With modulation, a swimmer that normally traces out a helical trajectory without any modulation is demonstrated to swim close to the channel's long axis in a straight trajectory.

The CFD studies model the swimmer with a cylindrical head and helical tail in a circular channel subject to Poiseuille flow. Force-free and torque-free swimming boundary conditions are applied to solve Stokes equations. One model assumes perfect synchronization of swimmer rotation with rotating magnetic field while the other one does not have such an assumption. One model predicts the average swimming behavior while the other one is a more detailed model which predicts full trajectory and velocity of the swimmer in a time-dependent fashion. The results of both models are compared with those of experiments.

2

METHODOLOGY

2.1. Experimental Setup

Microswimmers consist of a permanent magnetic cylindrical head and a helical tail, manufactured with a 3D-printer (Projet HD 3000) which uses VisiJet EX 200 polymers. Radially polarized neodymium-iron-boron ($Nd_2Fe_{14}B$) cylindrical permanent magnets, which are 0.4 mm in diameter and 1.5 mm in length, are adhered between the holders at the tip of the helical tail as the head of the swimmer (Fig. 2.1). Due to unavailability of VisiJet EX 200 polymer, previously available swimmers are used. Alongside these swimmers, new swimmers were ordered from 3rd party companies but they failed to swim due to their weight.
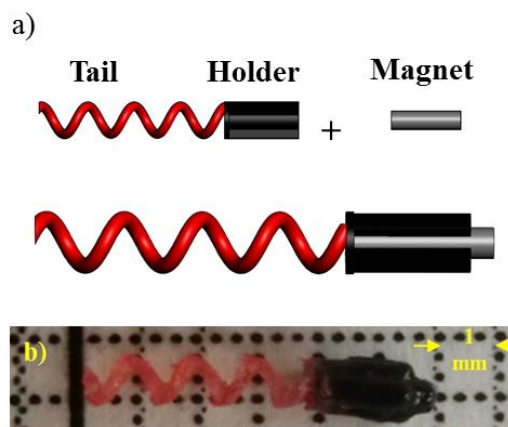
Fig. 2.1. a) Schematic representation of microswimmer fabrication, b) Real swimmer, with the tail length of 4 mm.

The experimental setup consists of 3 pairs of Helmholtz coils, each coil placed on sides of a cubic structure, shown in Fig. 2.2. The current passing through the coils are controlled by LabVIEW software by means of Maxon ADS_E 50/5 motor drivers and NI DAQ hardware. The software allows the user to input alternating current at desired frequency and amplitude. For a Helmholtz coil pair, the magnetic field at the center of the coil pair is given by:

$$B = \left(\frac{4}{5}\right)^{3/2} \frac{\mu_0 I N}{R_{he}} \tag{2.1}$$

where μ_0 is the permeability of free space, N is the number of turns in one coil, I is the amount of current passing through the coils and R_{he} is the radius of the coil, which is equal to the distance of each coil to their midpoint. The channel the swimmer is placed in is at the middle of the cubic structure. I, N and R_{he} values for each coil pair are tabulated at Table 2.1. Current values are set according to N and R_{he} parameters such that applied magnetic field of each pair is the same. There are two separate experiment groups with different current values. The calculations with the formula above give a magnetic field of $5.994 \cdot 10^{-3}$ Teslas for the first experiment group and $23.976 \cdot 10^{-3}$ Teslas for the second experiment group. The magnetic torque on the swimmer is calculated by:

$$\boldsymbol{\tau}_\mathbf{m} = \mathbf{m} \times \mathbf{B} \tag{2.2}$$

where $\mathbf{m}$ is the magnetization of the permanent magnet on the swimmer head, in A·m^2, Magnetization is calculated by multiplication of magnetic moment with the magnet volume:

$$\mathbf{m} = \mathbf{M}v \tag{2.3}$$

The magnetic moment is calculated from the coercivity of the material the magnet is made of. Neodymium magnets have coercivity ranging from 1 to 1.3 Tesla [45]. Assuming a value of 1, dividing this value with the permittivity of vacuum gives the magnetic moment and thus magnetization is found out to be $1.5 \cdot 10^{-4}$ A·m^2. So, the amplitude of magnetic torque is evaluated as $9 \cdot 10^{-7}$ N·m for the first group of experiments and $36 \cdot 10^{-7}$ N· m for the second group of experiments. Note that in these calculations it was assumed that there is no magnetization in **x-** direction. However, as soon as the swimmer loses its alignment with **x-** axis, magnetization in **x-** direction will no longer be zero and magnetic torque in **y-** and **z-** directions will appear.
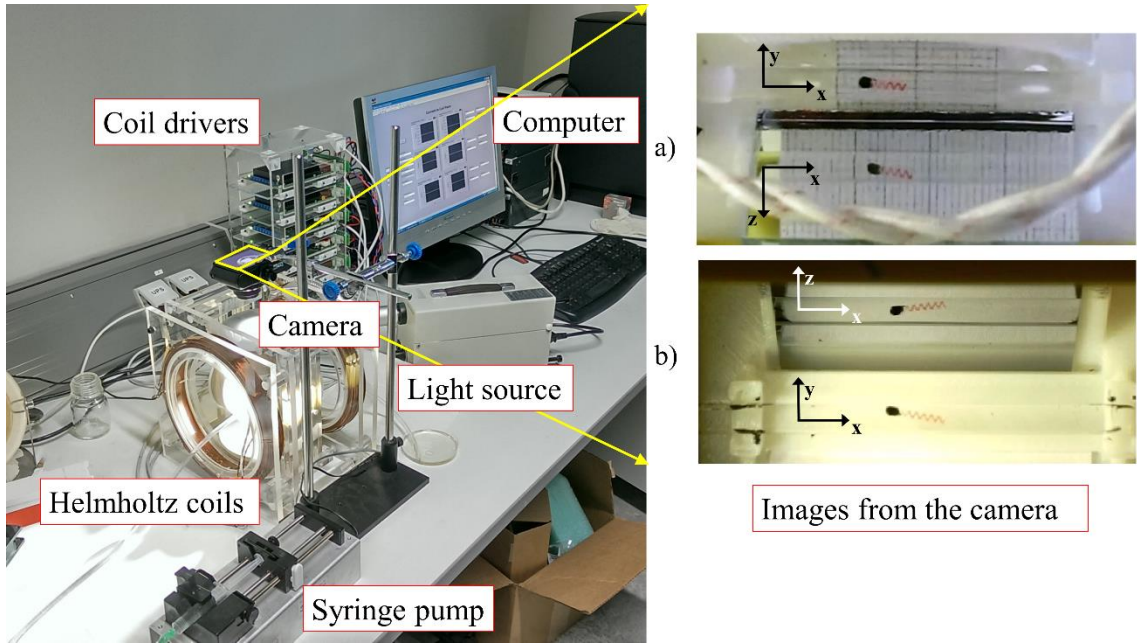
Fig. 2.2. Main components of the experimental setup. Inside of the experimental setup is shown through camera images alongside Cartesian coordinate axes placement. Capture a) is from the first group of experiments while capture b) is from the second group of experiments.

Table 2.1. Features of Helmholtz coil pairs

Coil	N	R_{he} (cm)	I (A)
1	750	2.25	0.2, 0.8*
2	500	3	0.4, 1.6*
3	250	3.75	-
*Underlined parameters are for the second group of experiments only.			

Note the components of magnetic field in Eq. (2.2) are sinusoidal and out of phase. By applying out of phase alternating current, rotating magnetic field is achieved, rotating the head of the swimmer. The rotation of the swimmer causes propulsion due to the swirling caused by the helical tail's rotation. The frequency of rotation for each pair is the same so that a perfect circular rotation is achieved. **x-** component of the magnetic field is equal to 0 so that the magnetic field vector is aligned with **x-** axis.

Glass cylindrical channels that experiments are conducted in are placed onto a support in the middle of the cubic structure. The support includes housing sections for the glass channel and also a 45-degree inclined plane to place a mirror which allows to track the swimmer in 3 dimensions. Two different glass channels are used in the scope of the thesis: One with an inner diameter of 1.6 mm and the other with an inner diameter of 3

mm. Each channel has a length of 10 cm. The channels are filled with glycerol which has a density of $\rho=1264$ kg·m^{-3} and a viscosity of $\mu=1.412$ kg·s^{-1}·m^{-1}. Both ends of the glass channels are connected to plastic tubing. One end of plastic tubing is connected to a syringe pump to supply flow into the system while the other end is left open. The experiments are recorded using CASIO EX-ZR1000 camera, as shown in Fig. 2.2, at 120 frames per second. Captures from the experiment recordings are shown in Fig. 2.2 alongside with Cartesian coordinate definitions for the setup. As one can see, x-y plane image is collected directly while x-z plane image is recorded through the reflection from the mirror placed with a 45-degree angle. Note that reflected image is upside down at Fig. 2.2. a) which affects coordinate axis placement.

There are two groups of experiment recordings. The first group is recorded earlier by Acemoglu [46]. The second group is recorded later with some modifications. The first difference between these two groups is the light source used. In the second group of experiments, a stronger light source -with a warmer color- is used. The second difference in the second group of experiments is the elimination of millimeter paper since it caused noise in data extraction, which will be explained further below. The third difference is in the mirror. There is a thick mirror in the first group of experiments. When this mirror was used with the new light source of second group of experiments, due to reflection from the sides of the glass tube, dark borders appeared at the edges of the channels, which posed challenges in data extraction. That's why the mirror was replaced with a silicon wafer in the second group of experiments. Though the image reflected is a little darker in tone, it resolves many problems the thicker mirror causes. Note that the placement of the mirror is changed as well such that the reflection is not upside down.

The swimmers used in these two groups of experiments also differ. In the first group of experiments, swimmers with tail lengths of 1.4 and 4 mm are used while in the second group of experiments swimmers with 3 and 6 mm tail lengths are used.

2.2. Image Processing of Experiment Videos

Recorded images of experiments are processed to obtain position and orientation of microswimmers using Image Processing Toolbox of MATLAB [47]. Code that is used for extracting the position and orientation on x-y plane are provided in APPENDIX: IMAGE PROCESSING CODE. Full-length experiment videos are cropped (in time) by video editing software to capture representative behavior and also to reduce the computational cost. The cropped videos last up to 10 seconds and generally it is more than enough to observe steady state behavior of the swimmers.

The algorithm works on each experiment video on a frame-by-frame basis. The algorithm first loads specified experiment video and saves the video on computer memory by separating it into frames. Next, the algorithm moves on to define a search region. The region is specified by two features, one being the channel boundaries and the other being swimmer size. Since one frame consists of two different images of interest, one showing x-y plane and the other showing x-z plane image (through reflection), the procedure explained below are carried out for both of the images separately at each frame (Refer to Fig. 2.2 for captures from experiments).

The channel boundaries are manually determined by visual inspection. In the first group of experiments, boundaries had to be selected thoroughly by checking nearly each experiment video as the boundaries could vary from one video to another while in the second group, the experiments were recorded at once so the boundaries remain the same. While the selection of boundaries is in an approximate fashion, and subject to error on the order of a single pixel size which is typically around 0.1 mm, the selected values can be verified in several ways. One of them comes from the unit pixel length. Unit pixel length is the length one side of a pixel occupies in terms of recorded environment. It is evaluated in different ways for different experiment groups. In the first experiment group, unit pixel length is determined from the millimeter paper placed in the setup by simply dividing total length of millimeter paper to the amount of pixels the paper occupies longitudinally. In the second set of experiments, unit pixel length is determined from the length of the mirror. Millimeter paper was not used in the second group of experiments as it caused noise in data extraction. After determining unit pixel length, channel boundary selection can be verified by calculating the diameter of the channel according

16

to those boundaries and comparing it with the actual channel size. Though this verification method ensures that channel boundaries are chosen in accordance with channel size, it does not ensure that boundaries are chosen properly as there is still a possibility that the channel centerline may be off compared to reality. To overcome this problem, an iterative scheme is employed where the trajectories of puller type swimmers, which are expected to be along the centerline of the channel, are examined. If the trajectory is off on the order of several times of unit pixel length, the boundaries are shifted accordingly and data is extracted again. While finding channel boundaries did not pose too much of a problem for the second group of experiments, it was challenging to come up with realistic results for the first group of experiments where the millimeter papers and low lightning caused difficulty in selecting the boundaries. Another problem seen mostly in the first group of experiments was the inclination of the channel in x-y and/or x-z planes. The inclination problem was either due to improper placement of the tube or improper placement of the camera. To overcome this issue, what was done was to determine channel boundaries from the region that the swimmer swims around. Since the videos are not very long and the swimmer mostly covers several millimeters of distance in **x-** direction throughout a video, the impact of this issue was observed to be not very significant; as there was no significant tilt in 3D trajectories of swimmers.

After the channel boundaries are selected both for the image in x-y plane and x-z plane, the second limitation on search region comes from swimmer dimensions. This limitation is applied as the frames are processed. The process will be explained in detail below. The algorithm requires two more parameters before starting which are related with the processing itself and will be recalled below. The algorithm starts processing a frame by cropping it according to the boundaries provided. Next, greyscale version of the cropped image is obtained. The contrast is increased. The histogram of this greyscale image is matched with the histogram of the greyscale image of the first frame of the video. With this step, a darker or lighter image can be adjusted according to the reference frame. The matched image is displayed alongside the original color image so that any possible error can be inspected (in Fig. 2.3).
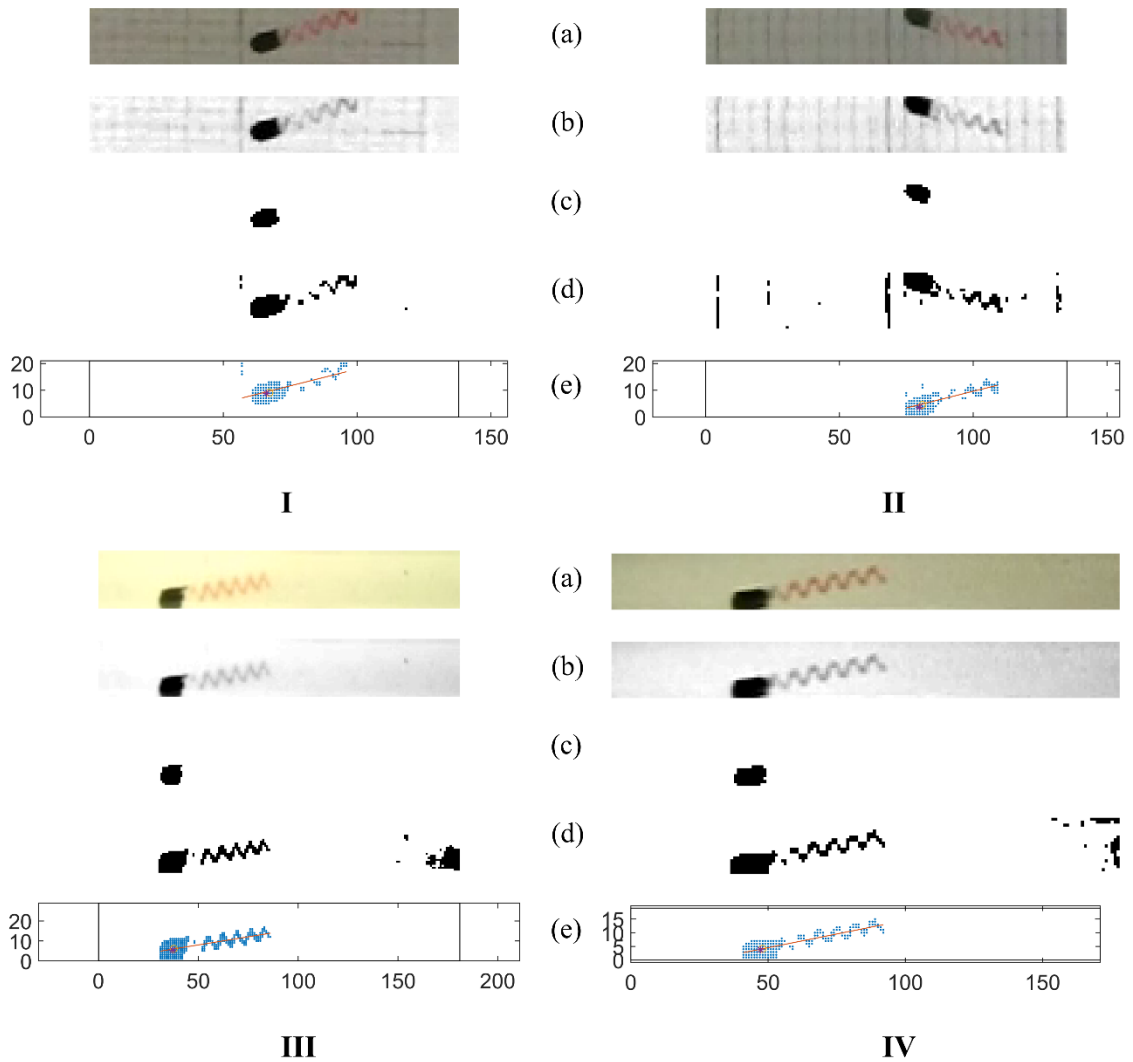
Fig. 2.3. The steps in data extraction. Image set I and II are from the first group of experiments and images III and IV are from the second group of experiments corresponding to x-y plane and x-z plane images, respectively. Note the improvement in the accuracy of data extraction in the second group of experiments.

After the grayscale image is obtained, two new binary images are generated with different threshold values. One of them is for extracting position of the swimmer head while the other one is for extracting the orientation of the swimmer. In this step, pixels with luminance greater than the threshold value are assigned a value of 1 while the rest is assigned a value of 0. So, darker regions have a value of 0. Since swimmer head is black, a low threshold value is enough to extract its region. On the other hand, extracting the tail profile (to extract orientation) requires a higher threshold as the luminance of the red tail is higher than the luminance of the black swimmer head. That's why there's a secondary threshold value which is used to extract the tail and head together. By assigning a low threshold value to find the swimmer head, any other possible noise within the image is

eliminated. Assigning a higher threshold to extract the tail in the first group of experiments posed a critical problem as the grid lines of the millimeter paper are extracted alongside the swimmer tail, some visible in section II at Fig. 2.3. Threshold limit is carefully adjusted for these videos so as to decrease noise as much as possible. For the second group of experiments, inhomogeneous lightning towards the further ends of the channel caused these regions to appear dark. The videos are cropped in time such that the swimmer is not around those regions.

After two images, one with the head and one with the head and the tail, are obtained, since black pixels correspond to a value of 0, logical not of both of the images are calculated so that they have a value of 1. The images are flipped upside down as well to transform the pixel coordinate system into the Cartesian coordinates defined above. Fig. 2.3 shows each step in processing with images from the first (I and II) and second experiment group (III and IV). I and III are x-y plane images while II and IV are x-z plane images. (a) is the cropped color image while (b) is the image coming from histogram matching for each set. (c) are the binary images coming from lower threshold (to find head coordinates) and (d) are the binary outputs from the higher threshold (to calculate orientation). (e) display the calculated centroid from lower threshold (red point) and the line fit to the points to find the orientation. While head is extracted from the image without a problem, extracting the tail profile brings in noise. Bounding the search region around the centroid of the head is helpful in eliminating the noise away from the swimmer, as can be seen in I and II. In III and IV, noise is minimized in both of the images. Note that image (e) in II is upside down compared to the original due to the placement of the mirror.

After obtaining images (c) and (d), the algorithm moves on to find two parameters: First one is the centroid of the swimmer head. For this, the centroid of the largest region in the first image (with low threshold) is evaluated. As can be seen in image (c), the largest region is the swimmer head itself. By specifying the largest region, we eliminate the possibility of noise being added into the calculation. After the centroid is calculated, the algorithm moves onto image (d), which includes the tail profile alongside the head. The algorithm first collects the positions of all black points found in image (d). Next, based on the centroid evaluated from image (c), the search region is bounded with respect to swimmer size: The points X_1 pixels to the left, X_2 pixels to the right, Y_1 pixels downwards and Y_2 pixels upwards of the centroid are the boundaries of the search region. With this step, noise away from the swimmer is eliminated, such as the points at the right end of

19

the image visible in Fig. 2.3 (e) at sections III and IV. However, there are cases where the swimmer is much more tilted than anticipated where the region Y_1+Y_2 pixels wide doesn't cover all of the tail. For such cases, the algorithm redefines Y_2 or Y_1 depending on the slope of the line fit to the points selected. If the slope of the line is positive, it means that the bounding box should be extended upwards so Y_2 is increased to

$$Y_{2new} = Y_2 + p_s X_2 \qquad (2.4)$$

where p_s is the slope of the line fit to the available points and X_2 corresponds to the length of the tail in pixels (just an estimation). If p is smaller than 0, this time the search region should be extended downwards:

$$Y_{1new} = Y_1 - p_s X_2 \qquad (2.5)$$

The points in this new bounding box are collected and a line is fit to these points. Inverse tangent of the slope gives orientation of the swimmer. θ_{xy} is the orientation angle obtained from x-y plane image while θ_{xz} is the angle obtained from x-z plane image, defined in Fig. 2.4. Obtained position and orientation data from the two planes are recorded in separate files for each experiment video.

Raw data is smoothed out with a moving average filter. Span of the filter depends on the amount of frames it takes for swimmer to complete one rotation, $120/f$. Depending on the absolute value of rotation rate, this value is adjusted further to improve smoothing performance such that span is mostly around 20 to 40 frames·s. The data still are raw as the swimmer position values are off due to diffraction of light from the cylindrical channel walls. Diffraction causes the midsection of the channel to appear wider and the regions nearby the channel walls smaller. This causes the swimmer to appear to have passed beyond the channel boundaries. To overcome this effect, following radial correction algorithm for a cylindrical jet is applied. The correction is based on trigonometry and Snell's law of refraction:

$$r_{sw} = r - \sqrt{R_{ch}^2 - r^2}\, \tan\left[\arcsin\frac{r}{R_{ch}} - \arcsin\frac{r}{n_{ref} R_{ch}}\right] \qquad (2.6)$$

where r is the radial position (raw) of the swimmer on y-z plane, R_{ch} is the total radius of the channel and n_{ref} is the refractive index of the medium, which is taken constant as 1.5 [48]. From r_{sw}, corrected **y-** and **z-** coordinates are obtained from

$$\begin{bmatrix} y \\ z \end{bmatrix}_{sw} = r_{sw} \begin{bmatrix} \cos(\theta) \\ \sin(\theta) \end{bmatrix} \qquad (2.7)$$

where

$$\theta = \mathrm{atan}\left(\frac{z}{y}\right) \qquad (2.8)$$

Swimming trajectories are discussed over the parameter β, evaluated from:

$$\beta = \frac{r - r_{mean}}{r_{sw} - R_{head}} \qquad (2.9)$$

where R_{head} is the radius of the head of the swimmer, r_{mean} is average radial position. With this definition, it is possible to tell how close or far the swimmer is from channel walls independently from channel diameter. A β value of 1 means that the swimmer head is touching the channel wall while a β value of 0 means that the swimmer is in center.
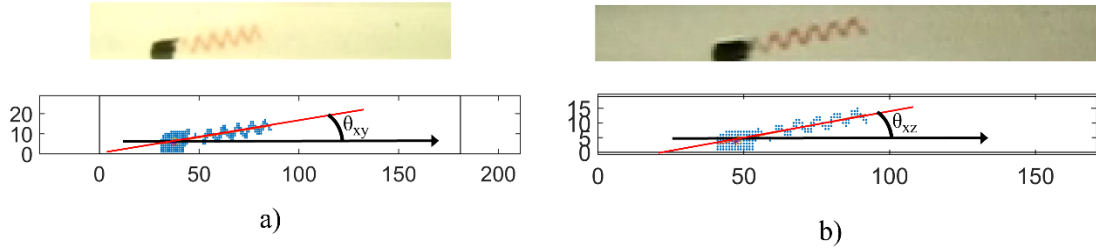
Fig. 2.4. Two angles, θ_{xy} and θ_{xz}, extracted from images in x-y plane (a)) and x-z plane (b)).

Due to the cylindrical symmetry of the motion, orientation of the swimmer in *x-y* and *y-z* planes are transformed to rotations about **r-** and **θ-** axes in cylindrical coordinates, θ_r and θ_θ as shown in Fig. 2.5. As can be seen in the figure, when **r-** and **z-** axes are coincidental, θ_{xy} is equal to θ_r and θ_{xz} is equal to θ_θ. For other cases, the local coordinate system consisting of **e₁-**, **e₂-** and **e₃-** axes (corresponding to new, local **x-**, **y-** and **z-** axes, respectively) should be defined such that new **r*-** and **e₃-** axes are coincidental. The tail coordinates of the swimmer in **y-** and **z-** directions in a neutral orientation are known. Applying θ_{xy} amount of rotation around **z-** axis and θ_{xz} amount of rotation around **y-** axis gives the swimmer tail position with respect to global coordinate frame (**x-**, **y-** and **z-**) Next, the rotation matrix that transforms **r** to **r***, R_{local} is evaluated. Rotating the tail profile with R_{local} gives the tail profile in local coordinate frame (**e₁-**, **e₂-**, **e₃-**). A line is fit to the tail coordinates in e₁-e₂ and e₁-e₃ planes to obtain $\theta_{xy}{}^*$ and $\theta_{xz}{}^*$ angles, which are equal to θ_r and θ_θ.
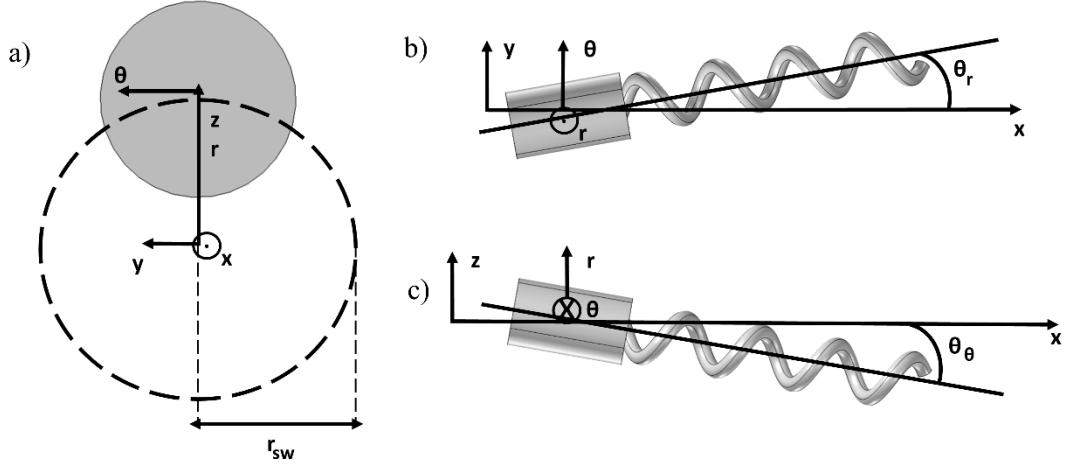
Fig. 2.5. Placement of swimmer such that **r-** and **z-** axes are aligned. r_{sw} denotes radial position of the swimmer. b) Top view of the swimmer from x-y plane, showing **θ-** and **r-** axes and also θ_r angle. c) Side view of the swimmer from x-z plane, showing θ_θ angle.

After θ_r and θ_θ are calculated, the only parameters that remain to be evaluated are velocities. Velocity in **x-** direction, (main direction of motion) u_{sw}, is evaluated by finding the slope of the fit line to position data as the change in **x-** position is linear. This is the mean velocity only. Variation between each frame is calculated as well to obtain maximum and minimum velocities. To eliminate noise in calculating the variation, **x-** position data is filtered with a higher span, twice of the original filter span. Lateral velocity, v_θ, is calculated from velocities in **y-** and **z-** directions:

$$v_\theta = v_{sw} \sin(\theta) - w_{sw} \cos(\theta) \qquad (2.10)$$

where v_{sw} and w_{sw} are velocities in **y-** and **z-** directions, respectively. Due to cyclic nature of motion in **y-** and **z-** directions, velocity calculation in those cases requires a fit consisting of sum of several sinusoidal functions. The derivative of the sum gives out the velocity profile.

2.3. Modulation of the Magnetic Field

By only employing two Helmholtz coils, a rotating magnetic field whose magnetization vector is aligned with the channel's long axis is obtained, shown in Fig. 2.6 a). The current given to coils placed on x-y and x-z plane are:

$$I_1 = I_A \sin(\omega t) \tag{2.11}$$

$$I_2 = I_B \sin(\omega t + \frac{\pi}{2}) \tag{2.12}$$

where I_A and I_B are the amplitude of the currents, given in Table 2.1, $\omega=2\pi f$ is the angular frequency of alternating current (referred to as rotation rate as well) and t is time in seconds. By incorporating a third pair of Helmholtz coils that are placed orthogonally to two pairs, the magnetic field can be modulated as desired. A few examples are provided in Fig. 2.6. The available LabVIEW program to control the current passing through the coils is developed further so that any kind of current can be supplied to third coil pair. The user can input any function depending on time and frequency with desired amplitude and phase difference. After testing out the effects of various functions on the swimmer, the program is modified such that it can provide different current profiles in a periodic fashion in order to account for different modulation necessities at different parts of swimmer trajectory.

$$I_3 = 0 \qquad\qquad I_3 = -\sin(\omega t) \qquad\qquad I_3 = -\cos(\omega t)$$
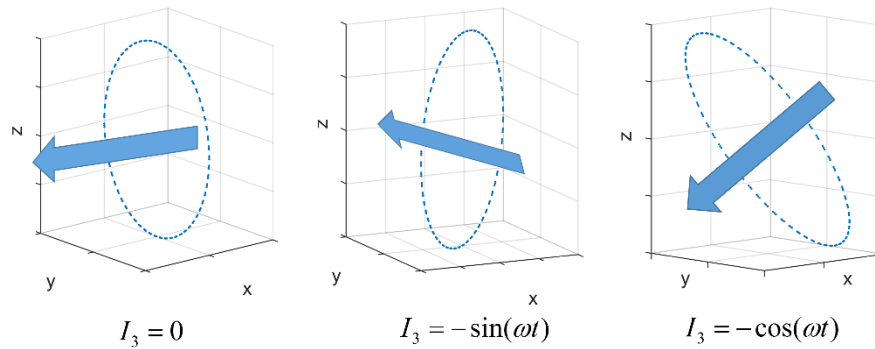
Fig. 2.6. Magnetic field without any modulation applied ($I_3 = 0$) and with modulation. I_3=-sin(ωt) results in a tilt in **+y** direction while I_3=-cos(ωt) results in a tilt in **-z** direction.

2.4. CFD Models

Having a cylindrical head and a left-handed rigid helical tail, the swimmer is placed axially inside a circular channel of diameter D_{ch} (see Fig. 2.7). The length of the tail is represented by L_{tail}, the overall length of the swimmer is L_o; the length and diameter of the head are L_{head} and D_{head}; wavelength and amplitude of the helical waves are λ and B_{sw}, and the diameter of the filament tail is D_{tail}. The geometric parameters and their values are tabulated in Table 2.2. The pusher and puller types (forward and backward) of motion of the swimmer with respect to the position of the head and the tail are depicted in the negative and positive **x-** directions respectively in Fig. 2.7.

The motion of the fluid surrounding the swimmer in the channel is governed by incompressible Stokes equations as the Reynolds number that correspond to the motion of the swimmer and the Poiseuille flow inside the channel are much less than unity.

$$\frac{1}{\text{Re}}\nabla^2\mathbf{u} - \nabla p = 0, \quad \nabla \cdot \mathbf{u} = 0 \tag{2.13}$$

where **u** and p are the nondimensional velocity vector and the pressure, respectively, and Re is the Reynolds number and equals to $\text{Re} = \rho L_{scale}^2 / \mu |f|$. In the nondimensionalization, the length scale, L_{scale}, is 1 mm, the time scale is the inverse of the magnitude of the rotational frequency of the magnetic field, $1/|f|$, and the pressure is nondimensionalized with the group $\rho L_{scale}^2 / f^2$.

No-slip boundary conditions are applied on the channel wall (u = 0 at $r = R_{ch}$) and at the surface of the swimmer, which moves with the velocity $\mathbf{V} = [U, V, W]'$, and rotates with the angular velocity vector, $\boldsymbol{\omega} = [\omega_x, \omega_y, \omega_z]'$, the velocity is specified as:

$$\mathbf{u} = \mathbf{V} + \boldsymbol{\omega} \times (\mathbf{x}_s - \mathbf{x}_{com}) \tag{2.14}$$

where $\mathbf{x}_s$ is the position of a point on the surface of the swimmer and $\mathbf{x}_{com}$ is the center-of-mass. Linear and angular velocities are obtained from additional constraint equations known as force-free and torque-free swimming conditions. The CFD model takes radial position and the orientation of the swimmer as input and calculates linear and angular velocities subject to external forces and torques such as gravity, contact forces and magnetic torques in **y-** and **z-** directions. The first CFD model which outputs snap-shot

24

solutions takes fluid forces into account only while the second CFD model includes gravitational, magnetic and wall contact forces in calculations.
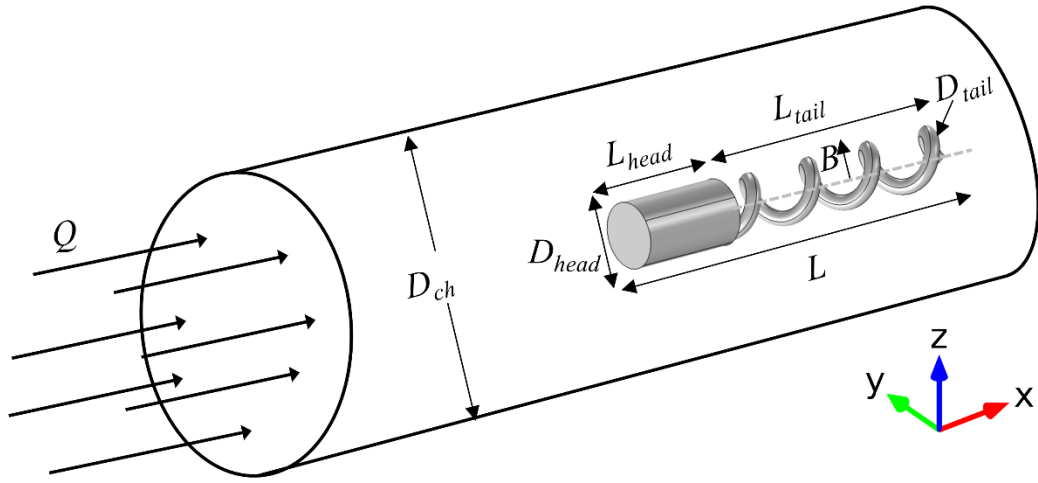
Fig. 2.7. Forward (head direction) and backward motion (tail direction) of the swimmer and geometric parameters of the swimmer model used in simulations.

Table 2.2. Geometric parameters of the swimmer in the simulations

Parameter	Values
Diameter of the cylindrical head, D_{head}	0.88 mm
Amplitude of the helical wave, B	0.4 mm
Length of the head, L_{head}	1.5 mm
Diameter of the tail, D_{tail}	0.2 mm
Length of the tail, L_{tail}	1.4 mm, 4 mm, 6 mm
Whole length of the swimmer, L	2.9 mm, 5.5 mm, 7.5 mm

Commercial software COMSOL is used to solve the system numerically with the finite element method [49]. The system has four main boundary conditions. The first two, no-slip condition at walls and moving wall condition at swimmer surface are described above. The third condition is the flow in the channel. Depending on flow direction, the flow is sent from one end of the channel. The final boundary condition is pressure point constraint of 0 Pa at the top of inlet surface.

2.4.1. Kinematic Model

Two basic equations to describe the swimmer motion are:

$$\frac{d\mathbf{x}}{dt} = \mathbf{u} \qquad (2.15)$$

$$\frac{d\mathbf{e_i}}{dt} = \boldsymbol{\omega} \times \mathbf{e_i} \qquad (2.16)$$

where $\mathbf{x}$ is the position vector of the swimmer in global coordinate frame, $\mathbf{u}$ is the velocity vector in global coordinate frame, i=1, 2, 3 and $\mathbf{e_i}$ vectors denote the local coordinate system of the swimmer and $\boldsymbol{\omega}$ is the angular velocity vector in global coordinates. Local and global coordinate frames are shown in Fig. 2.8. $\mathbf{u}$ and $\boldsymbol{\omega}$ are calculated from the instantaneous force balances in the CFD model based on position and orientation of the swimmer. In the first CFD model it is assumed that swimmer is in synchronization with rotating magnetic field, so ω_x is known.

Force and torque balances on the swimmer are expressed as follows:
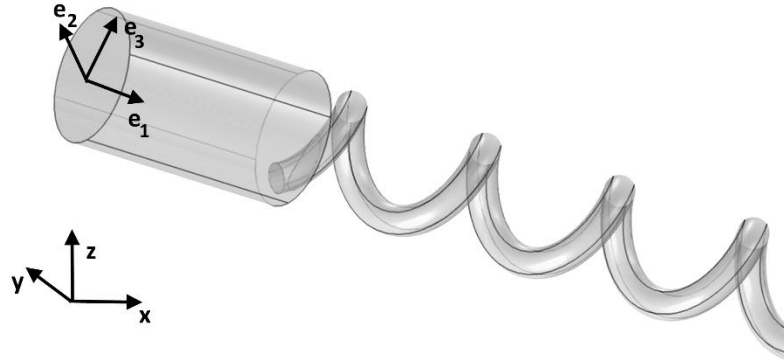
Fig. 2.8. Placement of local and global coordinate system.

$$\mathbf{F_f} + \mathbf{F_m} + \mathbf{F_g} + \mathbf{F_w} = 0 \qquad (2.17)$$

$$\boldsymbol{\tau_f} + \boldsymbol{\tau_m} + \boldsymbol{\tau_g} + \boldsymbol{\tau_w} = 0 \qquad (2.18)$$

Subscript f denotes fluid and the terms in Eq. (2.17) and (2.18) denote the force and torque the fluid exerts on the swimmer, respectively. Force of the fluid on the swimmer is calculated by:

$$\mathbf{F}_{f_j} = \oiint_S \sigma_{ij} \mathbf{n}_i dS \qquad (2.19)$$

26

where σ_{ij} for i = 1, 2, 3 and j = 1, 2, 3 are the elements of Cauchy stress tensor field and n_i denotes the components of normal of surface dS and S is the swimmer surface. The torque calculation requires center of mass of the swimmer, $x_{0,com}$. Note that due to the symmetric structure of the swimmer in local **y-** and **z-** directions, **y-** and **z-** coordinates of the center of mass is equal to 0 in terms of local coordinates at all times. Local **x-** coordinate of the center of the mass can be found by separately evaluating centers of mass of cylindrical head and helical tail and later evaluating the overall center of mass:

$$x_{0,head} = \frac{L_{head}}{2} \tag{2.20}$$

$$x_{0,tail} = \frac{L_{tail}}{2} + L_{head} \tag{2.21}$$

$$x_{0,com} = \frac{\rho_{tail} vol_{tail} x_{0tail} + \rho_{head} vol_{head} x_{0head}}{\rho_{tail} vol_{tail} + \rho_{head} vol_{head}} \tag{2.22}$$

For our case, it is assumed that $\rho_{head} / \rho_{tail} = 3$, which reflects the heaviness of the head due to the permanent magnet. The vector $x_{0,com}$ is defined as:

$$\mathbf{x_{0,com}} = \begin{bmatrix} x_{0com} \\ 0 \\ 0 \end{bmatrix} \tag{2.23}$$

And total torque exerted onto swimmer by fluid is calculated by:

$$\tau_f = \oiint_S (x - x_{0,com})\sigma_{ij}\mathbf{n_i}dS \tag{2.24}$$

Subscript *m* in Eq. (2.17) and (2.18) denote the magnetic force and torque. The swimmer is rotated with a rotating (in y-z plane) magnetic field. For a Helmholtz coil pair, the magnetic field at the center of the coil pair is given by Eq. 2.1. Nondimensional magnetic torque B_0 is obtained by:

$$B_0 = \frac{Bm_0}{\rho_{liq}L_{scale}^{5}f^{2}} \tag{2.25}$$

where m_0 is the magnetization of the magnet placed on the swimmer and L_{scale} is the length scale. Defining **m** as the unit magnetization vector of the swimmer, the magnetic moment applied to the swimmer is the cross product of this vector with the magnetic field vector:

$$\boldsymbol{\tau_m} = \mathbf{m} \times \mathbf{B} = \begin{bmatrix} m_x \\ m_y \\ m_z \end{bmatrix} x \begin{bmatrix} B_x \\ B_y \\ B_z \end{bmatrix} = \begin{bmatrix} m_x \\ m_y \\ m_z \end{bmatrix} x \begin{bmatrix} 0 \\ B_0 \cos(\omega t) \\ B_0 \sin(\omega t) \end{bmatrix} \qquad (2.26)$$

where ω is 2π for pusher mode and -2π for puller mode.

Subscript g denotes the gravitational force and torque in Eqs. (2.17) and (2.18). Nondimensional gravitational force is calculated separately for head and tail by:

$$F_{g,head} = -\frac{(g)(vol_{head})}{L_{scale}} t_{scale}^2 (\rho_{head} - \rho) \qquad (2.27)$$

$$F_{g,tail} = -\frac{(g)(vol_{tail})}{L_{scale}} t_{scale}^2 (\rho_{tail} - \rho) \qquad (2.28)$$

where g is the gravitational acceleration, t_{scale} is the time scale of the model, $1/f$, and ρ is non-dimensional density of the liquid. The density of the liquid is necessary in order to subtract the buoyancy force from the gravitational force. The negative signs in the expressions come from the direction of the gravitational force in global coordinate frame. Following a vectorial notation, gravitational torque can be calculated by:

$$\boldsymbol{\tau_{g,head}} = (\mathbf{x_{0,com}} - \mathbf{x_{0head}}) \times \begin{bmatrix} 0 \\ 0 \\ F_{g,head} \end{bmatrix} \qquad (2.29)$$

$$\boldsymbol{\tau_{g,tail}} = (\mathbf{x_{0,com}} - \mathbf{x_{0tail}}) \times \begin{bmatrix} 0 \\ 0 \\ F_{g,tail} \end{bmatrix} \qquad (2.30)$$

Subscript w denotes the force and torque exerted by the wall in Eqs. (2.17) and (2.18). When the swimmer is close to the channel wall less than r_{tail}, radius of the helical tail, the model assumes that the swimmer has hit the wall and as a reaction, applies a force in the opposite direction at the same amount of the force applied by the swimmer onto the fluid. Firstly, radial stress σ_r is expressed in terms of stress components in **y-** and **z-**directions:

$$\sigma_r = \sigma_{iy}\mathbf{n_i}\cos(\theta) + \sigma_{iz}\mathbf{n_i}\sin(\theta) \qquad (2.31)$$

where σ_{iy} and σ_{iz} are these stress components, respectively. Now that the radial stress is defined, it has to be integrated over the whole swimmer surface to obtain total force. However, there needs to be a Boolean check on whether the swimmer has hit the channel

wall R_{ch}-Δw away from the actual channel wall or not. Applying this Boolean check, the wall stress on the swimmer is calculated as:

$$\sigma_{wall} = \frac{F_r(F_r > 0)}{((\oiint_S (R_{ch} - r_{sw}) < \Delta w) + \varepsilon)} \tag{2.32}$$

where $F_r = \oiint_S \sigma_r dS$ is the net radial force outwards, and the Boolean expressions give 0 or 1 depending on whether the specific point on swimmer body is very close to the channel wall, ε is a small value to prevent division by 0 in case the specific point on the swimmer isn't beyond the imaginary wall. F_r>0 condition is put so as to apply a reaction force only if the net total radial force is outwards.

2.4.2. Numerical Implementation

This simulation model is used to simulate the swimmer motion in time by calling the CFD model to calculate velocities every time step. The first 2 or 4 seconds of swimmer motion are simulated based on whether steady state swimming is reached or not. The code simulates the swimmer at the instants Δt seconds apart. Δt is set to 1/750 or 1/300 seconds depending on swimmer mode. Since the swimmer moves towards channel walls in pusher mode, time steps taken have to be very small such that the collision physics can work properly to keep the swimmer within channel boundaries. In puller mode, however, the time step can be increased as the swimmer already moves close to the center of the channel.

Initialization consists of setting swimmer position and orientation. It is assumed that the swimmer starts its motion from somewhere near the bottom of the channel, considering gravitational effects. The swimmer is initially oriented along the channel's long axis. Thus the initial rotation matrix is a 3x3 identity matrix. 3-step Adams-Bashforth algorithm is employed to determine the next rotation matrix (to find out the orientation of the swimmer) and position of the swimmer. For a time step n (where $n \geq 3$), new position and orientation are calculated from:

$$R_{n+1} = R_n + \Delta t (\frac{23}{12} \omega_{\mathbf{n}} R_n - \frac{4}{3} \omega_{\mathbf{n-1}} R_{n-1} + \frac{5}{12} \omega_{\mathbf{n-2}} R_{n-2}) \tag{2.33}$$

$$\mathbf{r}_{n+1} = \mathbf{r}_n + \Delta t(\frac{23}{12}\mathbf{u}_n - \frac{4}{3}\mathbf{u}_{n-1} + \frac{5}{12}\mathbf{u}_{n-2}) \tag{2.34}$$

in which $\mathbf{r}$ is the position vector of the swimmer and $\mathbf{u}$ and $\boldsymbol{\omega}$ are the linear and angular velocity vectors, respectively. Subscripts denote the time steps. For the first and second time steps, forward Euler and two-step Adams-Bashforth methods are used:

$$R_1 = R_0 + \Delta t(\boldsymbol{\omega}_0 x R_0) \tag{2.35}$$

$$\mathbf{r}_1 = \mathbf{r}_0 + \Delta t(\mathbf{u}_0) \tag{2.36}$$

$$R_2 = R_1 + \Delta t(\frac{3}{2}\boldsymbol{\omega}_0 R_0 - \frac{1}{2}\boldsymbol{\omega}_1 R_1) \tag{2.37}$$

$$\mathbf{r}_2 = \mathbf{r}_1 + \Delta t(\frac{3}{2}\mathbf{u}_2 - \frac{1}{2}\mathbf{u}_1) \tag{2.38}$$

After the evaluation of the new rotation matrix R_{n+1}, the matrix is normalized using singular value decomposition. After normalization, Euler angles are extracted from the rotation matrix and the swimmer is oriented as necessary. The model takes these new position and orientation data as input and outputs linear and angular velocities for the algorithm to find out the initial orientation and position of the swimmer for the next simulation. Since translation in **x-** direction doesn't have any effect on swimming dynamics, the swimmer is assumed to stay in the center of the channel in **x-** direction in the simulation. Depending on the resulting velocity in **x-** direction, the position is calculated and stored in MATLAB software.

Fluid domain is discretized with tetrahedral elements while triangular elements are used for the head and the tail of the swimmer. Maximum element size of the swimmer body is kept lower in order to better capture the complicated shape of the swimmer. Three boundary layers are placed for the first CFD model while the second model doesn't have any boundary layers. For the swimmer with the tail length of 4 mm, number of degrees of freedom is 82957 with 99580 elements. A convergence test is applied by selecting a random instant from time-dependent simulation model. The results are tabulated in Table 2.3. Assuming that the densest mesh gives the most accurate result, the meshing used deviates 3-4%. Considering that over 1500 separate simulations have to be carried out for one configuration, simulation time has to be kept as short as possible as well. In that regard, the meshing chosen gives close enough results with much lower computation time compared to the most accurate simulation.

Table 2.3. Convergence test for the second CFD model. The line in bold is the meshing used for simulations.

Number of domain elements	Degrees of freedom	Computation Time [s]	Error in u_{sw} [%]	Error in v_{sw} [%]	Error in w_{sw} [%]
23849	21252	9	-27.8	-6.71	-14.2
56430	47092	24	-10.1	9.22	-5.55
80999	66515	41	-8	4.36	-8.16
99580	**82957**	**55**	**-4.22**	**8.51**	**-8.18**
130408	108312	90	-3.54	11.42	-8.64
657524	536096	1082	0*	0*	0*
*Error rate of solution with the finest mesh is taken as 0 and other error percentages are calculated based on the results from there.					

With this simulation model, it is possible to observe both transient and steady state behavior of the swimmer. It is also possible to change magnetic field as desired to observe swimmer behavior under different kinds of magnetic field.

3

SWIMMING CHARACTERIZATION

This chapter presents the results of swimming characterization on swimmer tail length, channel diameter and fluid flow by investigating swimmer trajectory, orientation and velocity. The results of the first kinematic CFD model are presented throughout the chapter, with the results of the time-dependent model discussed at the end as a separate subsection.

3.1. Swimmer Trajectory

Table 3.1 lists the range of parameters varied in the experiments. In order to easily refer to an experiment set, a compact notation system is introduced where letter D stands for channel diameter, L stands for swimmer tail length in mm and Q stands for the flow rate in mL/min for a reference channel with 1 mm diameter. As an example, D1.6-L4-Q20 refers to the experiment in the channel with diameter 1.6 mm, with the swimmer with a tail length of 4 mm at the average flow velocity of 0.414 mm/s in +**x** direction. In experiments, flow rate is varied to keep the average velocity the same for channels with different diameters.

Table 3.1. Varied parameters and identifiers in the experiments.

Parameter	Values	Identifier	Description
Angular velocity of the rotating magnetic field, $\pm 2\pi f$	$0 < f < 25$ Hz	-	Negative values indicate clockwise rotation (CW), positive values counter clockwise (CCW).
Channel Diameter, D	1.6 mm	D1.6	Narrow channel, diameter of 1.6 mm
	3 mm	D3	Wide channel, diameter of 3 mm
Swimmer Tail Length, L	1.4 mm	L1.4	Tail length of 1.4 mm
	3 mm	L3	Tail length of 3 mm
	4 mm	L4	Tail length of 4 mm
	6 mm	L6	Tail length of 6 mm
Parameter for the flow rate of the Poiseuille flow, Q	0	Q0	Average flow velocity, 0 mm/s
	± 10	Q10, Q-10	Average flow velocity, 0.207 mm/s
	± 20	Q20, Q-20	Average flow velocity, 0.414 mm/s
	± 30	Q30, Q-30	Average flow velocity, 0.621 mm/s

Experiment sets D1.6-L1.4-Q0, D1.6-L4-Q0 and D3-L4-Q0 are to be discussed in this section, with their trajectories presented in Fig. 3.1. Results for one experiment set are provided in each row of the figure. The plots in the first column illustrate the 3D trajectory of pusher mode swimming and the second column shows the puller mode swimming for the reference case of 15 Hz rotation rate. The plots in the third column display β values across all rotation rates. The blue dots denote the mean value while the bars extend to maximum and minimum values recorded for each experiment. The fourth column shows the lead values of helical paths for $\omega_x > 0$. The reason negative rotation rates are not included in the figure is due pullers ($\omega_x < 0$) following either straight or non-helical trajectories, so these trajectories lack a lead definition.

In the forward swimming mode, the swimmer with the left-handed helical (LHH) tail is rotated in the CCW direction and follows a right-handed helical (RHH) trajectory which is in the direction of rotation. Rotation of the swimmer due to the magnetic torque induces a strong swirling flow in the circular channel. The swimmer is carried by the rotating flow around itself due to its rotation by magnetic torque. Moreover, the CFD model confirms that the lateral velocity of the swimmer is in the direction of the rotating flow. Helical trajectories of swimmers in the forward direction are typical for the pusher mode swimming as reported for rigid spherical swimmers inside circular channels and also in living organisms [35, 39, 15]. Puller trajectories, on the other hand, are straight lines in the narrow channel. In the wider channel, the swimmer starts to follow a non-

straight path. Though it resembles a helical trajectory, it is not a fully developed one. From this observation, it can be stated that increasing channel diameter causes the puller to act like a pusher.
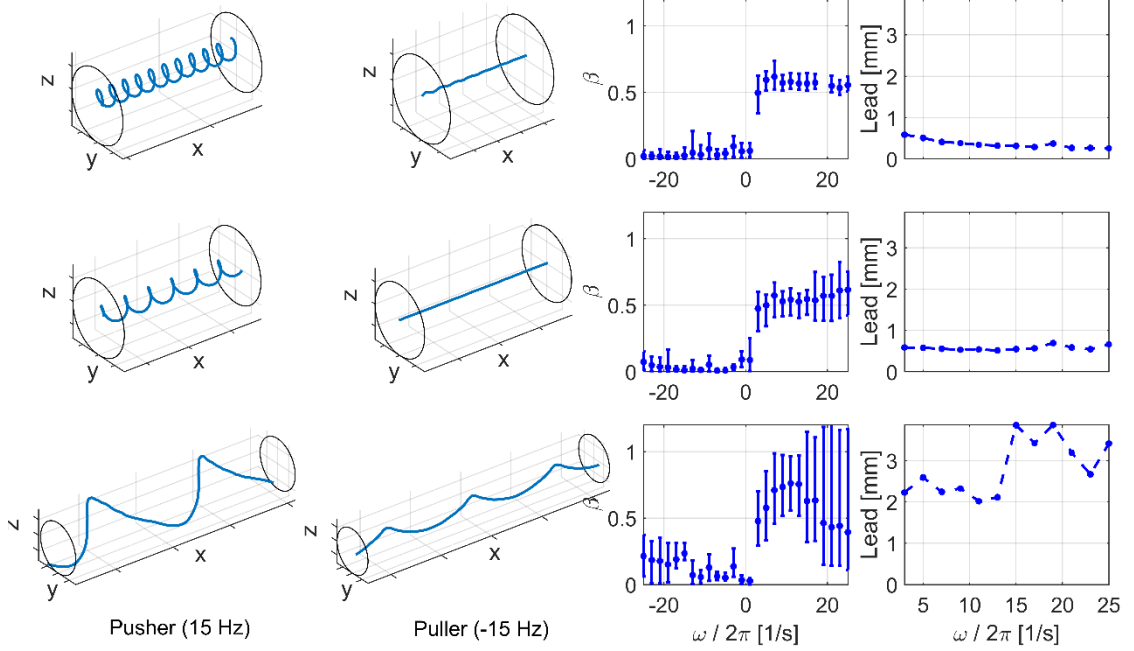
Fig. 3.1. 3D swimmer trajectories for pushing and pulling modes; lead values and β values across rotation rates for experiment sets D1.6-L1.4-Q0 (a) to d)), D1.6-L4-Q0 (e) to h)) and D3-L4-Q0 (i) to l)). Arrows indicate direction of motion.

Looking at β values, it should be noted that there are some cases where maximum passes beyond 1. This is a rare occurrence due to imperfections in data extraction explained in section Image Processing of Experiment Videos. Pullers follow not only a straight trajectory but also they stay close to channel's centerline while the pushers circulate around the centerline with higher variation in values than pullers. Note the increase in β at low rotation rates, this is due to inability of swirling flow in lifting up the swimmer head, which sinks to the bottom of the channel due to its weight when $\omega_x=0$. Compared to swimmer L1.4, L4 swims slightly closer to the center in pusher mode due to increased stability coming from the additional weight of the longer tail. Putting L4 in a wider channel results in an increase in β values overall: The swimmer swims further away in comparison to the swimmer in the narrow channel.

Before discussing lead values, their significance should be explained properly. Lead tells us how tight (small magnitude) or relaxed (high magnitude) a helical path is. So, lead values show the relation between u_{sw} and v_θ values. There is not much variation in lead values within experiment sets across rotation rates. While it takes much shorter time for

the swimmer to complete one helical rotation (due to increased ω_x) which decreases the lead value, the swimmer also travels much faster in propulsion direction which increases the lead value. The results indicate that these two factors balance each other. A short tail means a small lead value while a longer tail means a higher lead value due to enhanced propulsion. At the wider channel, lead values increase dramatically as the swimmer has more space to move in y-z plane so one helical rotation takes much longer time to complete. This observation is consistent with the higher β values as well. Lastly, note the sudden jump in helical lead value at D3-L4-Q0 experiment set at ω_x=15 Hz. This is due to step-out: It takes longer time for swimmer to complete one helical rotation so the swimmer covers more distance in propulsion direction, which means an increase in lead.

Another defining feature of swimmer trajectory is the orientation of the swimmer body and tail. In previous work, it was assumed that the swimmer is aligned with the channel's long axis in average [24]. This time, orientation of the swimmer is extracted from the videos and this assumption is found out to be true indeed. This is expected due to cyclic nature of swimmer motion. However, moving beyond average values and investigating swimmer orientation further, a significant difference is observed between experiment sets. Fig. 3.2 displays swimmer trajectories projected onto y-z plane (sampled), with black dots standing for swimmer head and red lines representing swimmer tail. The projections of helical paths closely resemble a circle but they slightly deviate from perfect circles. The main reason for deviation is the swimmer hitting channel boundaries. What's more important is that there is an L/D dependency on the way the pushers follow the helical trajectory: If L/D ratio is large, the tail is aligned towards the center of the channel at all times, meaning that the swimmer head follows the helical trajectory (as in D1.6-L4). If L/D is small, the tail is oriented towards the channel boundaries, showing that the head and tail move together through the helical trajectory (as in D1.6-L1.4 and D3-L4). The significance of this observation is that the best practice in terms of controlled swimming turns out to place a long swimmer inside a narrow channel as the tail stays oriented towards the center of the channel which is helpful in stabilizing the swimmer motion. Also note that while puller tail is aligned with the channel's long axis in the narrow channel, in the wider channel, puller and pusher orientation are very similar, as discussed above.
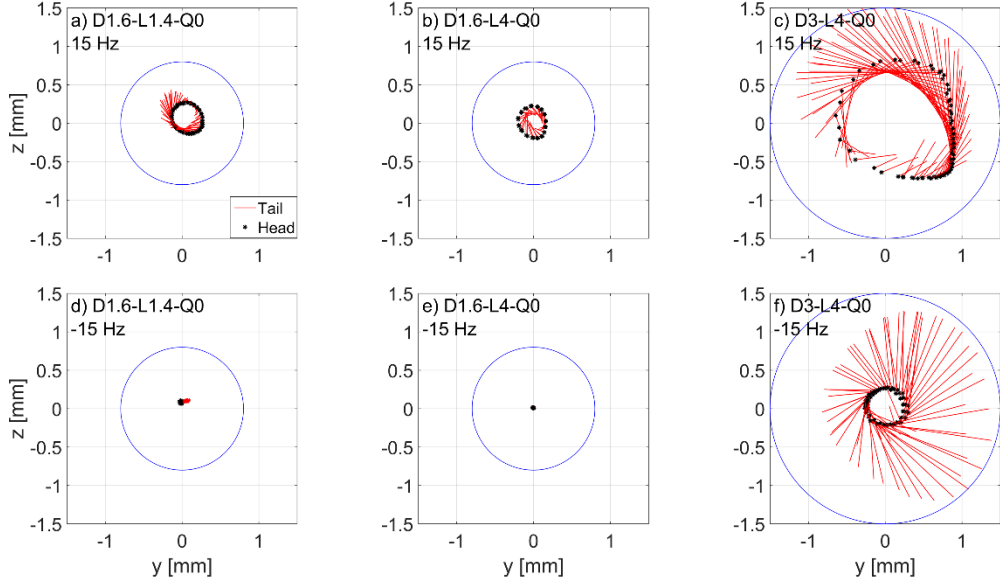
Fig. 3.2. y-z images of trajectories of pushers and pullers, showing swimmer head (in black) and tail (in red). Note the tail length of swimmer L1.4 is scaled by 2 for visibility. Blue circle indicates channel boundaries.

3.2. Effect of Flow on Trajectory

Effect of flow on swimmer trajectories will be discussed in two different ways. Firstly, the effect of amount of flow on the experiments discussed in the previous section will be examined. Second, the effect of the flow direction on the swimmer trajectories will be revealed from the results of second group of experiments, introduced in Section 2.1.

Fig. 3.3 displays the trajectories of the swimmers subject to flow in **+x** direction such that the pushers are swimming against the flow while the pullers are swimming in flow direction. All plots are for ω_x=15 Hz. Note that puller trajectories are not presented as there's no significant change in their 3D trajectories under flow. The direction of motion is shown with an arrow at the top of each subplot. Each row corresponds to one experimental configuration under four different flow rates, with the first row displaying the trajectories for D1.6-L1.4 experiments, the second displaying D1.6-L4 experiments and the third displaying D3-L4 experiments. The first observation on these plots is that increasing the flow rate leads to instability in trajectories, hinting at the increased wobbling. The next observation is that swimmer is able to swim against higher flow rates

in wider channels, given that swimmer L4 can't swim against the maximum flow velocity in the narrow channel but it can swim against the same flow velocity in the wider channel. This is due to decrease in wall shear effects on the swimmer.
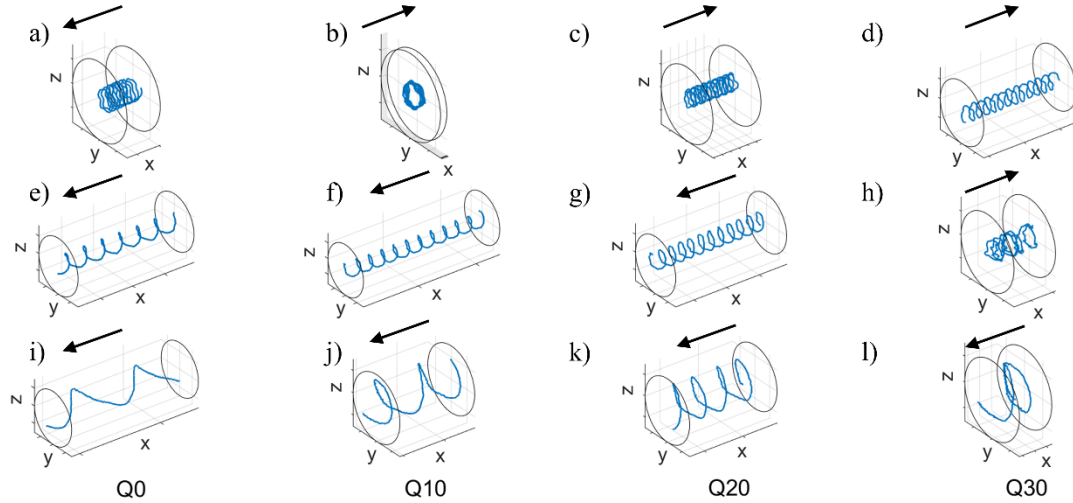
Fig. 3.3. Change of trajectories of swimmers under flow. First row displays the results for D1.6-L1.4 experiments, second row shows the results for D1.6-L4 experiments and the last row shows D3-L4 experiments. Flow rate is written at the bottom of each column (in compact notation). Arrows indicate swimming direction.

Values of β for the same experiments are provided in Fig. 3.4. From positive rotation rates in these plots, it can be seen that increase in the flow decreases β at D1.6-L1.4 experiments while there is an increase at D1.6-L4 experiments and at D3-L4 experiments there is no significant change. So, it can be concluded that there is an L/D dependence on the effect of flow on β values. A small L/D (D1.6-L1.4) indicates a decrease while a high L/D (D1.6-L4) means an increase. L/D-dependency means that the change in β is related with the orientation of the tail in the channel, discussed in Section 3.1. Note that no such effect is observed in the puller mode: β is generally very low at the experiments in the narrow channel according to experiments. In the wider channel, average β values and variation increase with increasing flow.
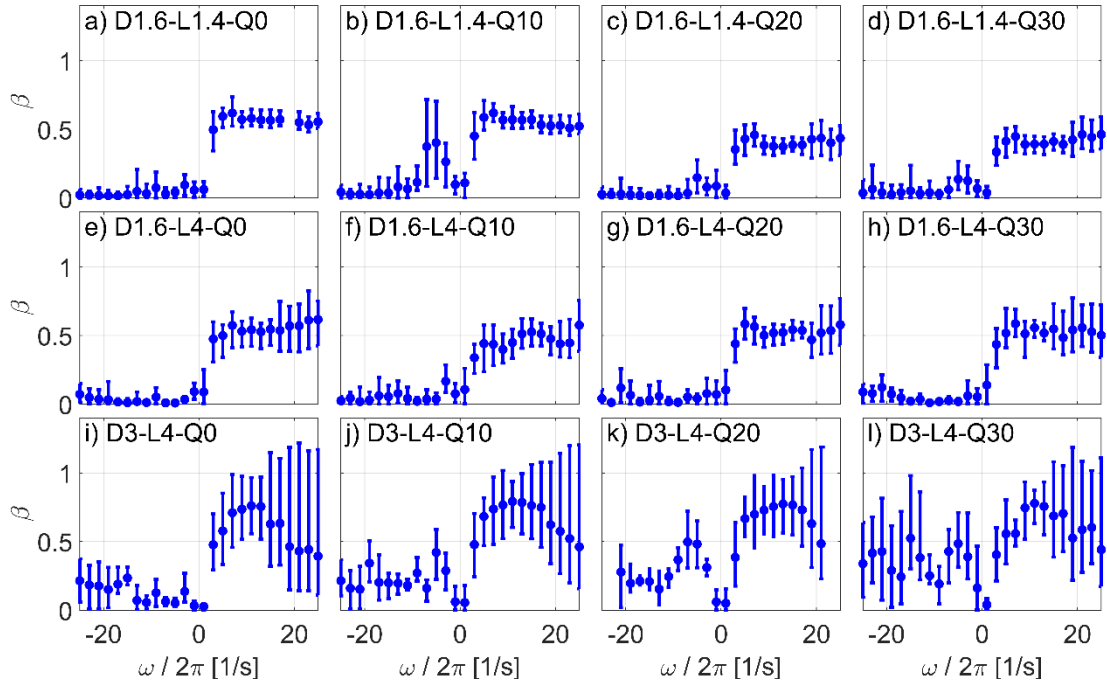
Fig. 3.4. β values in experiments with and without flow.

Lead values of the same experiments are provided at Fig. 3.5. Dashed lines at the plots are placed to distinguish swimmer motion against flow (positive lead) and in flow direction (negative lead). Since the positive rotation rates are investigated only, a negative lead value means the swimmer is not able to swim against the flow while a positive value means otherwise. Lead values, especially at low rotation rates decrease significantly with increasing flow. At D1.6-L4 and D3-L4 experiments with flow, while the lead increases to positive values, at high rotation rates, lead values start decreasing again. This is due to step-out behavior leading to a decrease in propulsion of the swimmer. This effect is visible especially in Q30 experiments.
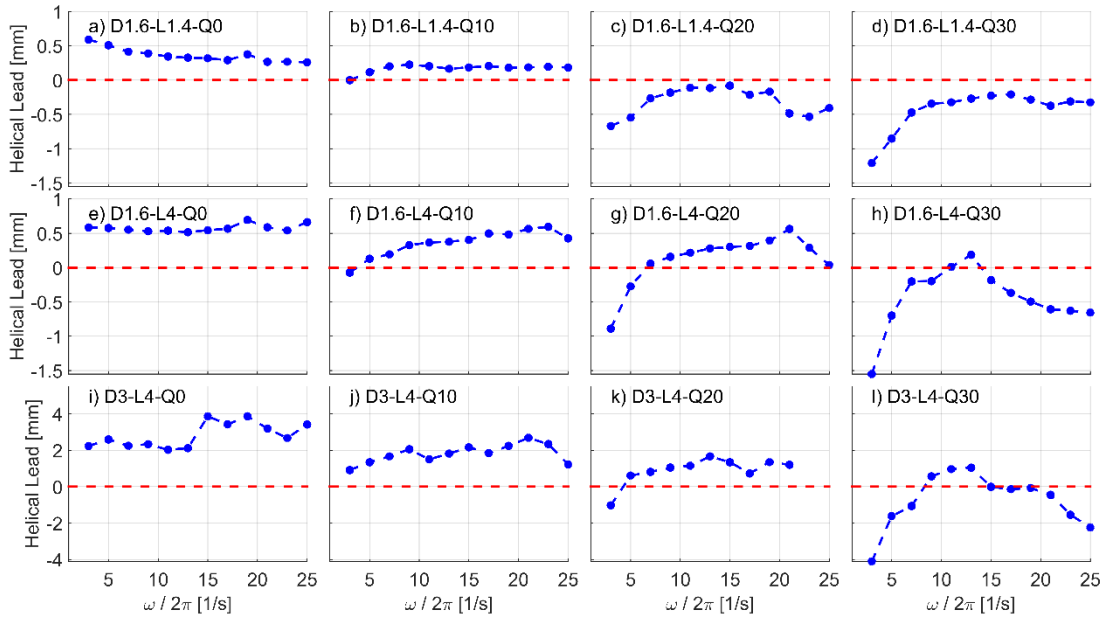
Fig. 3.5. Lead values of helical trajectories across four different flow rates.

Direction of the Poiseuille flow in the channel is expected to influence the trajectories of the swimmer. In the second group of experiments to be discussed, same amount of flow rate is given in +**x** and -**x** directions. Flow given in +**x** direction is in the direction of puller propulsion (also the direction of the flow in the experiments discussed above) while the flow given in -**x** direction is in the direction of pusher propulsion. Firstly, experiments conducted in the narrow channel (1.6 mm diameter) with swimmer L6 will be discussed. While there is no visual difference in 3D trajectories, (not shown) β values shown in Fig. 3.6 exhibit some key differences. Reversing the flow direction from +**x** to -**x** results in an overall increase in variation of β values. In other words, pushing the swimmer from the tail increases the instability of the swimmer. When flow is given in -**x** direction, the swirling flow the tail causes by rotation is mixed with Poiseuille flow. When flow is in +**x** direction, however, the swimmer head cuts the mixing of Poiseuille flow field and swirling flow field to some extent, which explains the higher stability. Direction of the flow is observed to have no effect on the alignment of the tail in these experiments.
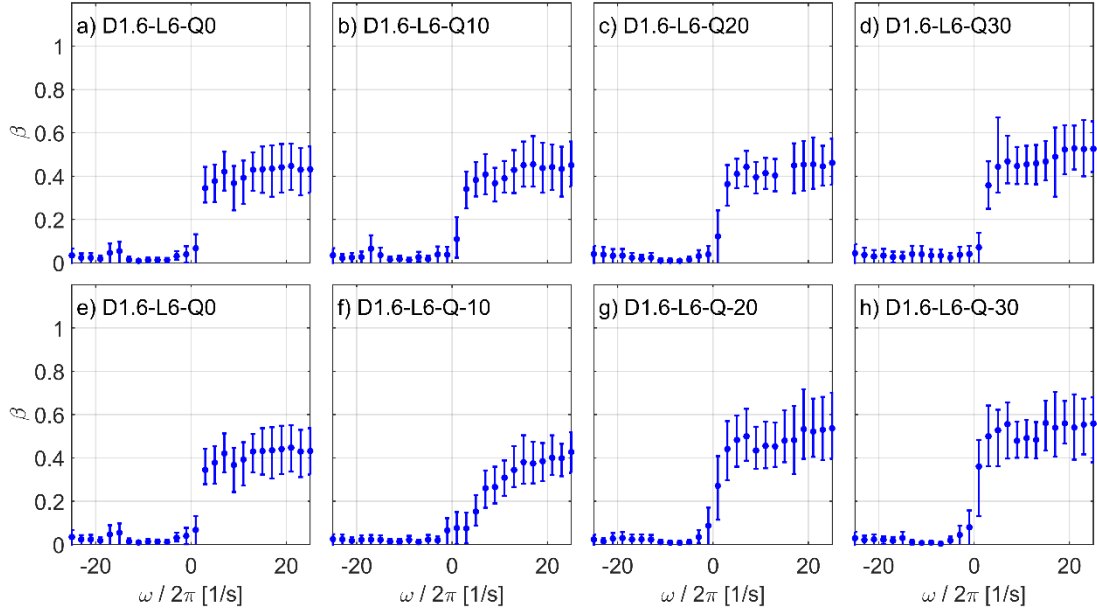
Fig. 3.6. β values of swimmers in D1.6-L6 experiments with opposite flow directions. First row shows the results for flow in **+x** direction while the second row shows the results for flow in **-x** direction.

Considering that L/D ratio is very large in D1.6-L6 experiments, greatly reducing the space that the swimmer can move, another group of experiments is carried out with the hope that other effects of flow direction may be observed. Fig. 3.7 shows β values for D3-L6 experiments with flow in both directions. Note the drop in β at pusher mode from low rotation rates towards higher rotation rates when the flow is in **+x** direction. β is initially high at low rotation rates due to gravitation. As rotation rate increases, swimmer starts moving closely around the channel's long axis. If rotation rate is increased further, β value jumps back to high values. Meanwhile, no such increase or decrease occurs when the flow is in **-x** direction. The profile in general is similar to D3-L4 experiment results given in Fig. 3.4. This may arise the question on why the general trends of D3-L4 and D3-L6 experiments at positive flow rates differ. The answer to this lies in L/D ratio as the decrease in β in pusher mode is observed when there is no flow at all. So, this decrease in β is not because of flow direction but rather due to L/D ratio. The increase in β values at high rotation rates point out to increased instability of the swimmer due to faster rotation. No significant difference in tail positioning is observed when flow direction is reversed. The amount of change in lead is comparable between opposing directions of flow, shown in Fig. 3.8. However, the amount of change in lead at low rotation rates is much more when flow is in **-x** direction, meaning that flow from tail side is more effective on the swimmer.

40
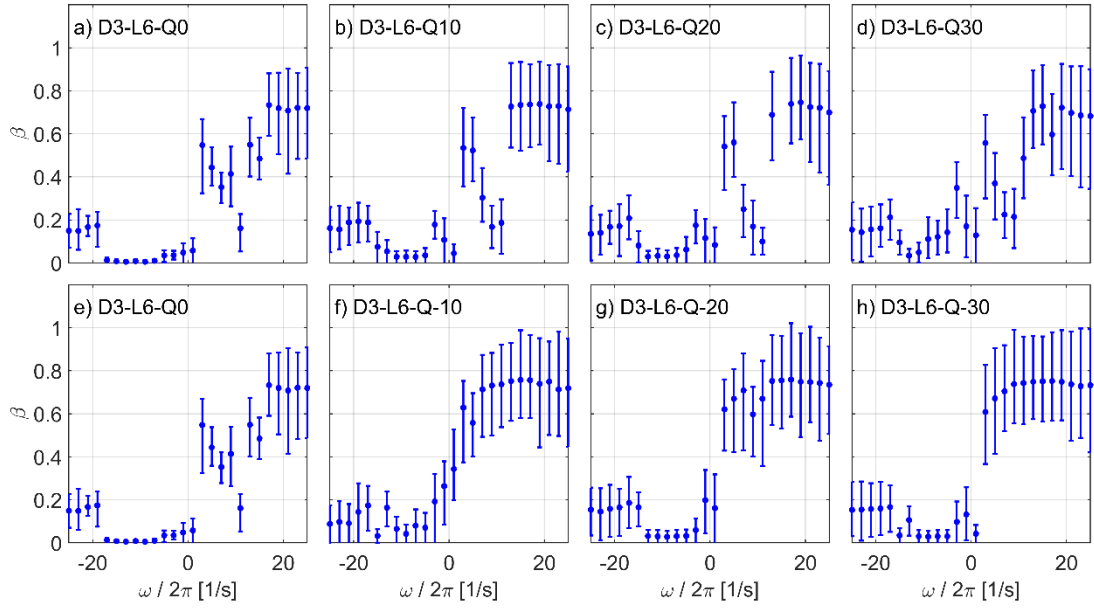
Fig. 3.7. β values of swimmers in D3-L6 experiments with opposite flow directions. First row shows the results for flow in +**x** direction while the second row shows the results for flow in -**x** direction.
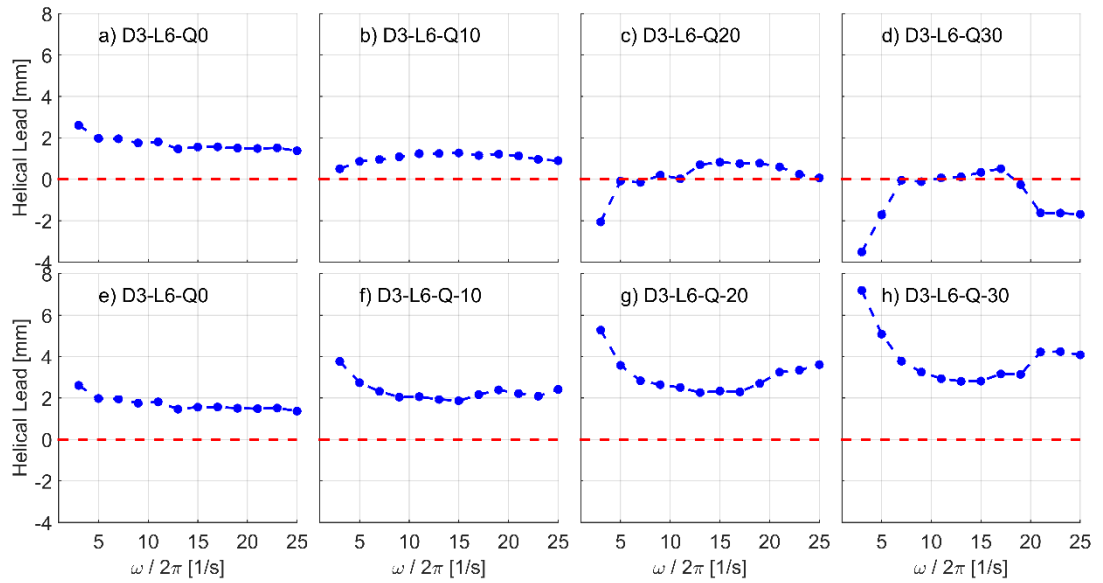
Fig. 3.8. Lead values for D3-L6 experiments.

3.3. Swimming Velocity

3.3.1. Propulsion Velocity

Propulsion velocity, u_{sw}, in this thesis is taken to be the velocity of the swimmer in **x-** direction, which is the main propulsion direction. As a reminder, the swimmer propels in **-x** direction in pusher mode and in **+x** direction in puller mode. The propulsion velocity results for the first three experiment sets (without flow) discussed in Section 3.1 are presented in Fig. 3.9 (in blue) alongside with the kinematic simulation results (in red). Note that not all simulation results for all rotation rates are available since the swimmers were out of channel boundaries based on the obtained values from experimental measurements. This is expected as there is an error band of unit pixel length, i.e., around 0.1 mm. Before comparing experiment and simulation results, a few observations on experiment results shall be discussed. In D1.6-L4-Q0 experiments, step-out is clearly visible at both ends of the rotation rate range as the swimming velocity decreases in magnitude. Step-out is much more visible at D3-L4-Q0 as the step out begins around 15 Hz rotation rate. The reason step-out is observed at D1.6-L4-Q0 case (considering there is no step out at D1.6-L1.4-Q0) is the increased weight while the decrease in step-out frequency at D3-L4-Q0 comes from the increased channel diameter as the swimmer is less confined so it is harder for the swimmer to stay synchronized with the rotating magnetic field; whose torque causes enhanced disorientation.
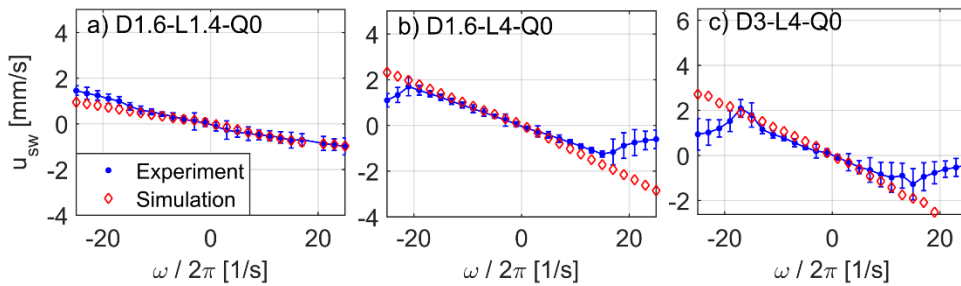
Fig. 3.9. Comparison of simulation and experiment result of propulsion velocities in experiments without flow.

Comparing the experimental observations with computational simulations, it is observed that the simulation results follow the experimental ones very closely in puller mode. However, in pusher mode, there is an increasing discrepancy as the rotation rate increases. This simulation model assumes the swimmer is always in sync with the rotating

magnetic field. However, when step-out occurs, such an assumption is not valid. Thus, a steady increase in velocity (in magnitude) is observed in simulations even for ω_x in which step-out occurs.

3.3.2. Effect of Flow on Propulsion Velocity

Values of u_{sw} at four different flow rates are displayed in Fig. 3.10, alongside the simulation results. Since flow is against the propulsion direction of pushers, a decrease in swimming velocity of pushers is observed with increased flow. Swimmer L1.4 cannot swim against the flow at high flow rates. At the experiments in the narrow channel, a suppression in step-out behavior is observed as there is no step-out in puller mode for swimmer L4 while in the pusher mode step-out rotation rate increases. Note that at the highest flow rate step-out comes back indicating that there is a limit in flow suppressing step-out behavior. Simulation results, as discussed in the previous section, follow the experiment results closely in the puller-mode while the discrepancy in the pusher-mode is observed in the cases with flow.
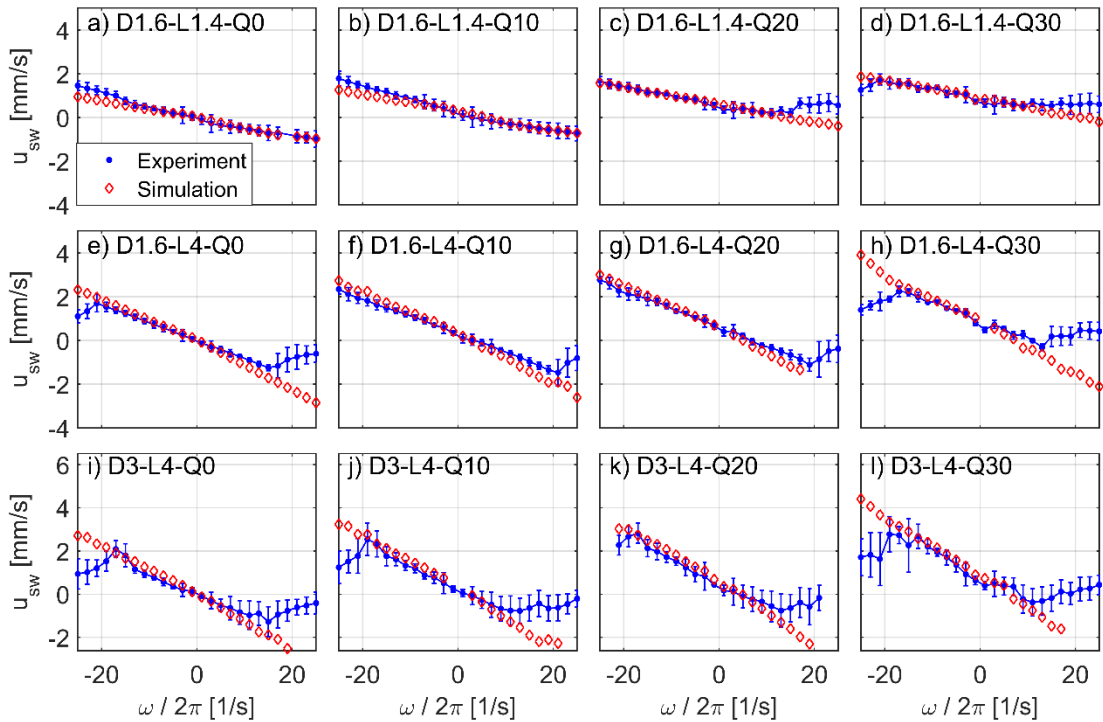
Fig. 3.10. Comparison of swimming velocities of experiments and simulations (with flow).

Having observed that flow in +**x** direction delays step-out in puller mode, one asks how the flow in -**x** direction would affect step-out. Fig. 3.11 displays u_{sw} values for experiments in both flow directions. According to the figure, flow in -**x** direction decreases the step-out rotation rate in both puller- and pusher- modes. As discussed before, flow given in tail side increases the instability of the swimmer, increasing wobbling and causing the swimmer to lose its synchronization with the magnetic field much more easily. Another important point in comparing the effect of the flow direction is the contribution of the flow to maximum swimming velocity. When the flow is in +**x** direction, which is expected to speed up pullers, maximum u_{sw} rises from 2.896 mm/s (with no flow) to 3.388 mm/s (D3-L6-Q20), a %16.9 increase. On the other hand, when the flow is in -**x** direction, which is expected to speed up pushers, maximum $|u_{sw}|$ rises from 1.374 mm/s (D3-L6-Q0) to 1.654 mm/s, a %20.3 increase. So, while it is argued that flow in -**x** direction is unfavorable in terms of swimming trajectory, it compares favorably in terms of increasing swimmer propulsion. On the other hand, u_{sw} in puller mode is hindered by flow in the -**x** direction significantly as there is a nearly %40 drop in maximum value when the flow in +**x** direction is reversed while the decrease in magnitude of u_{sw} is much less, around %20, in pusher mode when flow direction is reversed. This is thought to be related with mixing of fluid flow and swirling flow.
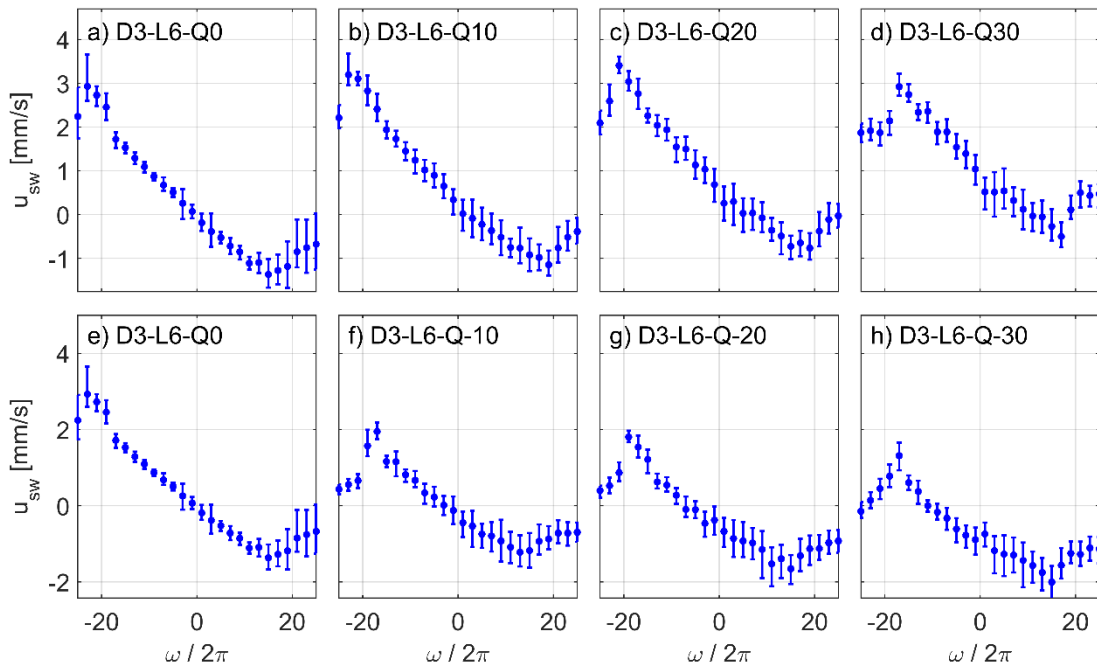
Fig. 3.11. Swimming velocity from experiments with flow in +**x** (a-d) and -**x** (e-h) directions.

3.3.3. Lateral Velocity

Velocity of the swimmer in the tangential direction in channel's coordinates is significant in terms of the helical trajectory of the swimmer. Moreover, the step-out is easily visible in v_θ values in pusher mode. Results are presented in Fig. 3.12 for the first group of experiments with snap-shot simulation results (for $\omega_x > 0$) obtained from average position and orientation of each swimmer. The swimmer is displaced in only **z-** axis in the model as representative of its radial position, then lateral velocity of the swimmer in **-y** direction is equal to its tangential velocity in Eq. 2.10. When the swimmer is close to the centerline of the channel, its tangential velocity does not have a significant meaning; therefore, simulation results for $\omega_x < 0$ are not included. The tangential velocity increases with the frequency up to the step out frequency and after step-out becomes prominent it decreases. Note that the increase in the tangential velocity is linear. The decrease after step-out, on the other hand, is exponential. Since the swimmer is very close to center in puller mode, lateral velocity converges to 0. The simulation results follow the experiments closely in the narrow channel, especially at rotation rates where no step-out occurs. The discrepancy in u_{sw} in Fig. 3.10 between the experiment and simulation results is in agreement with the discrepancy observed here. For the experiments in the wide channel, the simulation and experiment results are much more disconnected; the velocities are close to each other only at low rotation rates.
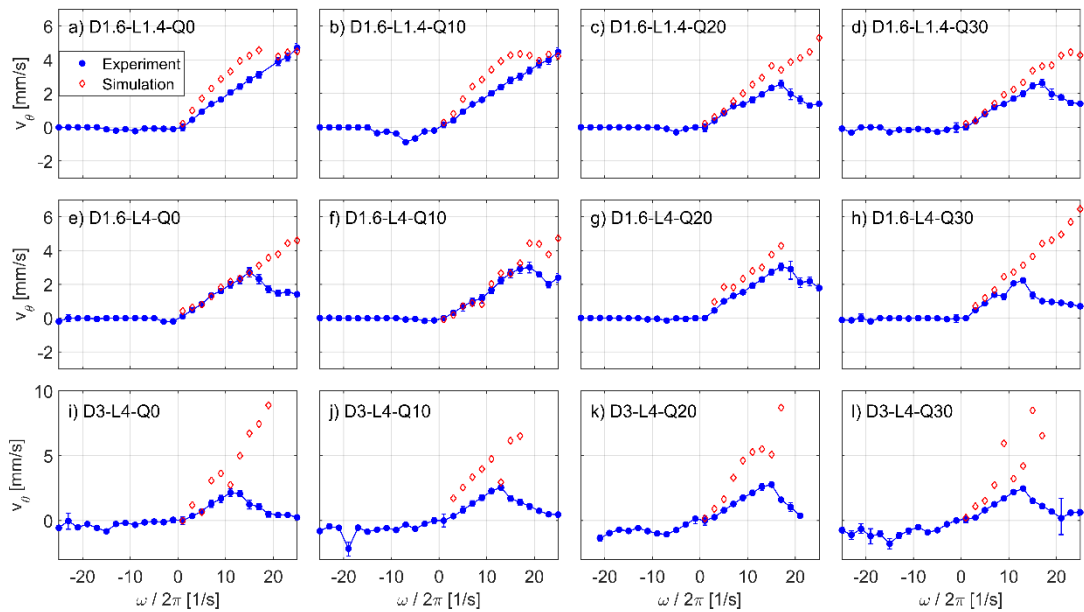
Fig. 3.12. v_θ values in the first group of experiments.

Now that flow's effect on the swimmer's rotation is observed, it is worth investigating the effect of the direction of the flow on the tangential velocities. The results for D3-L6 experiments are given in Fig. 3.13. Flow from the tail side (**-x** direction) reduces v_θ significantly. In general, when flow is from the tail side, there is more variation in the values. As observed in section Effect of Flow on Propulsion Velocity, step-out frequency is decreased as well. The abrupt jumps in values when flow rate is positive is related with the sudden jumps observed in β values in Fig. 3.7.
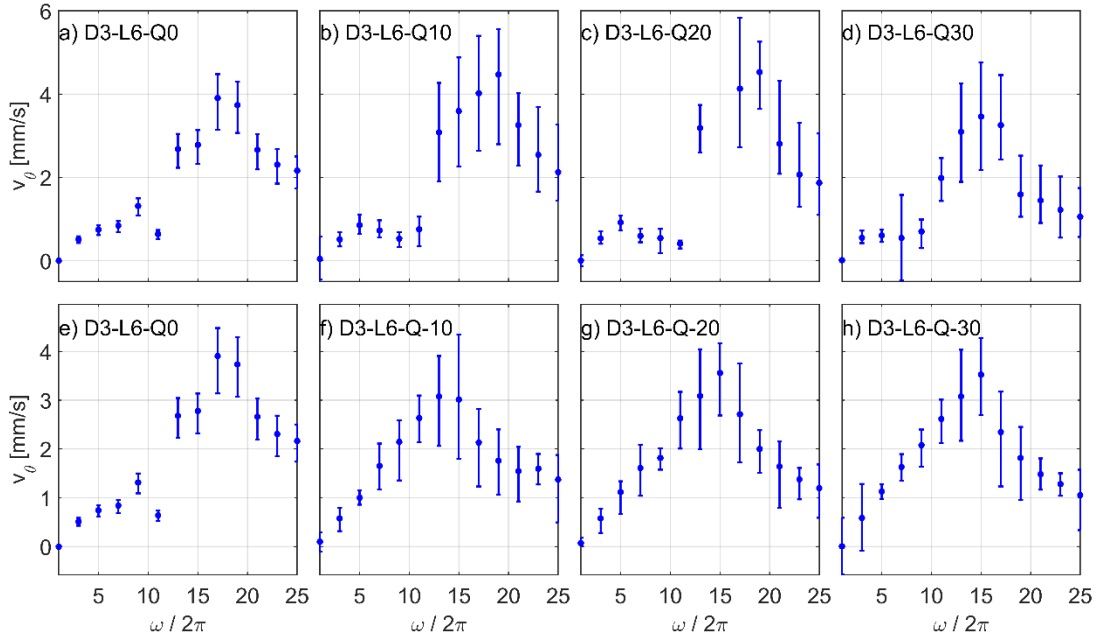
Fig. 3.13 v_θ values in the second group of experiments where we can observe the effect of flow direction.

3.4. Results of Time-Dependent Simulations

The results of time-dependent simulations described in Section 2.4 are reported in this subsection. Fig. 3.14 presents the 3D trajectories and swimming velocities calculated from the simulations for D1.6-L1.4 configuration alongside the experimental counterparts for comparison. First two columns are for pusher mode and last two columns are for puller mode at 15 Hz. To easily distinguish the trajectories, 3D trajectories of experiments and simulations are concatenated back to back in **x-** direction as a shift in position of the swimmer in **x-** axis does not cause any change in the context. Below this figure are lead values of the trajectories of experiments and simulations in Table 3.2 and below that are

46

u_{sw} and v_θ results, shown in Table 3.3. In the pusher-mode, the simulation follows experimental observations in terms of β at low flow rates. With increased flow, β in simulations increase but experiments tell otherwise. Lead is much smaller in simulations than in experiments. Just as in experiments, the swimmer is not able to swim forward after Q20. u_{sw} results are very close in average but variation is higher in simulations. The difference can be attributed to the geometric imperfections of the real swimmer that may potentially lead to different realization of ω_x.
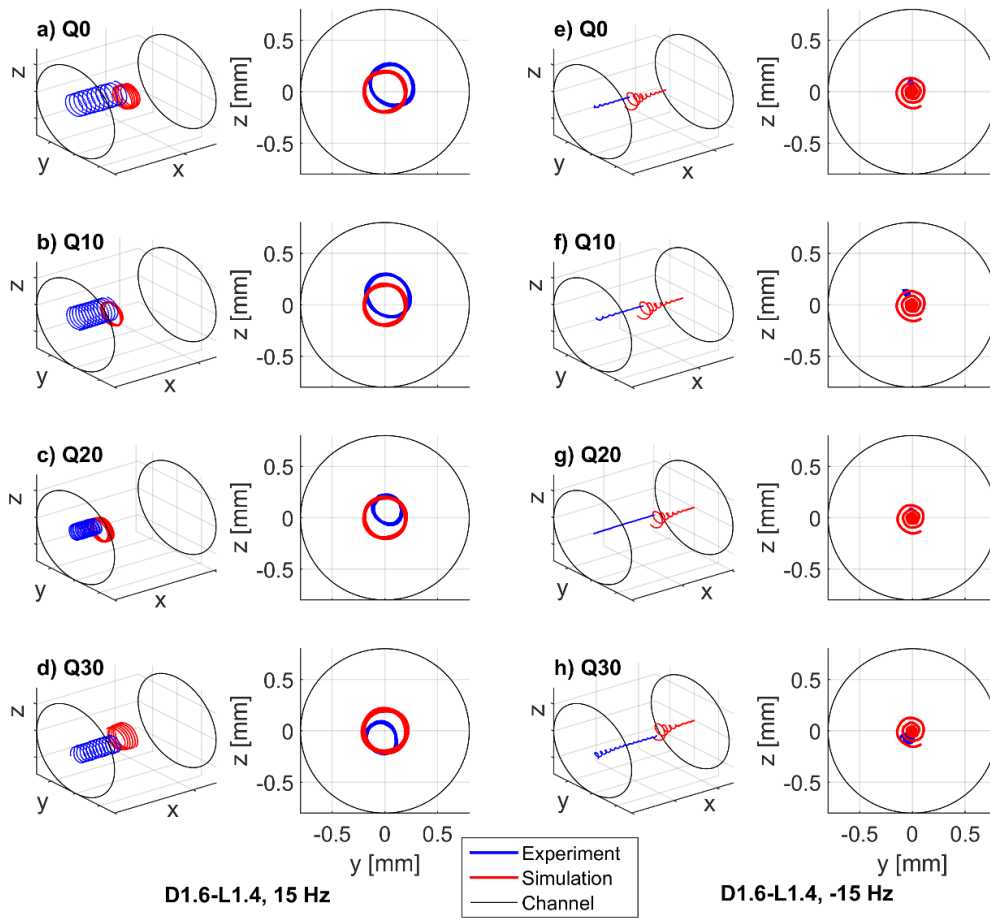
Fig. 3.14. Trajectories of simulations (in red) compared to experiment results (in blue) for D1.6-L1.4 configuration. a) to d) show pusher mode, e) to h) show puller mode.

Table 3.2. Comparison of lead values of D1.6-L1.4 experiments and simulations.

Experiment set	Lead value (Experiment)	Lead value (Simulation)
D1.6-L1.4-Q0, 15 Hz	0.317 mm	0.142 mm
D1.6-L1.4-Q10, 15 Hz	0.183 mm	0.05 mm
D1.6-L1.4-Q20, 15 Hz	-0.08 mm	-0.054 mm
D1.6-L1.4-Q30, 15 Hz	-0.229 mm	-0.135 mm

Table 3.3. Comparison of velocity values of D1.6-L1.4 experiments and simulations.

Experiment set	u_{sw} (Experiment)	u_{sw} (Simulation)	v_θ (Experiment)	v_θ (Simulation)
D1.6-L1.4-Q0, 15 Hz	-0.714 mm/s	-0.3519 mm/s	2.823 mm/s	3.662 mm/s
D1.6-L1.4-Q10, 15 Hz	-0.4037 mm/s	-0.0847 mm/s	2.795 mm/s	3.675 mm/s
D1.6-L1.4-Q20, 15 Hz	0.2023 mm/s	0.1772 mm/s	2.339 mm/s	3.694 mm/s
D1.6-L1.4-Q30, 15 Hz	0.5543 mm/s	0.4379 mm/s	2.45 mm/s	3.832 mm/s
D1.6-L1.4-Q0, -15 Hz	0.7646 mm/s	0.7505 mm/s	-0.1186 mm/s	-0.778 mm/s
D1.6-L1.4-Q10, -15 Hz	1.168 mm/s	1.043 mm/s	0 mm/s	-0.7522 mm/s
D1.6-L1.4-Q20, -15 Hz	1.167 mm/s	1.336 mm/s	-0.001 mm/s	-0.684 mm/s
D1.6-L1.4-Q30, -15 Hz	1.614 mm/s	1.632 mm/s	-0.2923 mm/s	-0.7285 mm/s

In the puller-mode, the swimmer traces out a helical trajectory with exponentially decaying amplitude that converges to a straight line at the center. This transient behavior is actually in line with the observations in the experiment results. However, as the transient swimming is cropped out from the recordings, the similarities cannot be observed. u_{sw} values are much closer this time to experiment results with much less variation.

Results for D1.6-L4 simulations in Fig. 3.15 agree with the experiment results more accurately than the results for D1.6-L1.4 configuration in terms of trajectory. Lead values for the pusher-mode (given in Table 3.4) in these simulations are very close to experimental observations. One major difference is that the swimmer is able to swim against flow Q30 in simulation but not in experiment. u_{sw} values (given in Table 3.5) in average are close to experiments but variation is very high. Fig. 3.16 shows u_{sw} and v_θ in simulation D1.6-L4-Q0, 15 Hz. There are sudden jumps in velocity values periodically. These jumps are correlated with the instants that the swimmer hits the channel walls. Contacts with the channel walls cause these jumps, with the swimmer rotating in the other direction and slightly moving back compared to propulsion direction as the force pushes away the swimmer from the boundary. If these spikes are omitted, the simulation results for u_{sw} follow the experiments closely, as can be seen from the average values, showing that the collision model is functional without disrupting the system much. On the other hand, average v_θ values tend to be higher in magnitude once again.
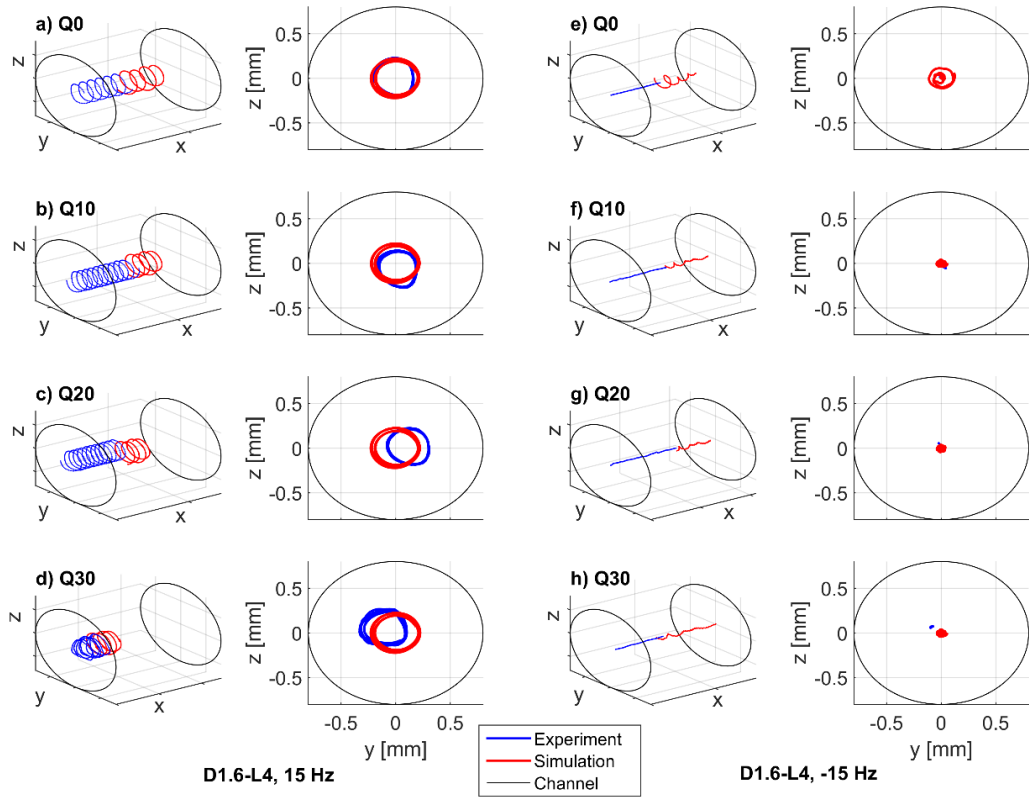
Fig. 3.15. Trajectories of simulations (in red) compared to experiment results (in blue) for D1.6-L4 configuration. a) to d) show pusher mode, e) to h) show puller mode.

Table 3.4. Comparison of lead values of D1.6-L4 experiments and simulations.

Experiment set	Lead value (Experiment)	Lead value (Simulation)
D1.6-L4-Q0, 15 Hz	0.545 mm	0.682 mm
D1.6-L4-Q10, 15 Hz	0.404 mm	0.512 mm
D1.6-L4-Q20, 15 Hz	0.302 mm	0.333 mm
D1.6-L4-Q30, 15 Hz	0.183 mm	0.262 mm

Table 3.5. Comparison of velocity values of D1.6-L4 experiments and simulations.

Experiment set	u_{sw} (Experiment)	u_{sw} (Simulation)	v_θ (Experiment)	v_θ (Simulation)
D1.6-L4-Q0, 15 Hz	-1.25 mm/s	-1.297 mm/s	2:737 mm/s	2.598 mm/s
D1.6-L4-Q10, 15 Hz	-0.9707 mm/s	-1.005 mm/s	2.659 mm/s	2.574 mm/s
D1.6-L4-Q20, 15 Hz	-0.6699 mm/s	-0.6958 mm/s	2.738 mm/s	2.5 mm/s
D1.6-L4-Q30, 15 Hz	0.1787 mm/s	-0.4208 mm/s	1.362 mm/s	2.525 mm/s
D1.6-L4-Q0, -15 Hz	1.232 mm/s	1.543 mm/s	0 mm/s	-0.9122 mm/s
D1.6-L4-Q10, -15 Hz	1.48 mm/s	2.01 mm/s	0 mm/s	-0.4049 mm/s
D1.6-L4-Q20, -15 Hz	1.877 mm/s	2.314 mm/s	0 mm/s	-0.3662 mm/s
D1.6-L4-Q30, -15 Hz	2.19 mm/s	2.604 mm/s	0 mm/s	-0.3775 mm/s
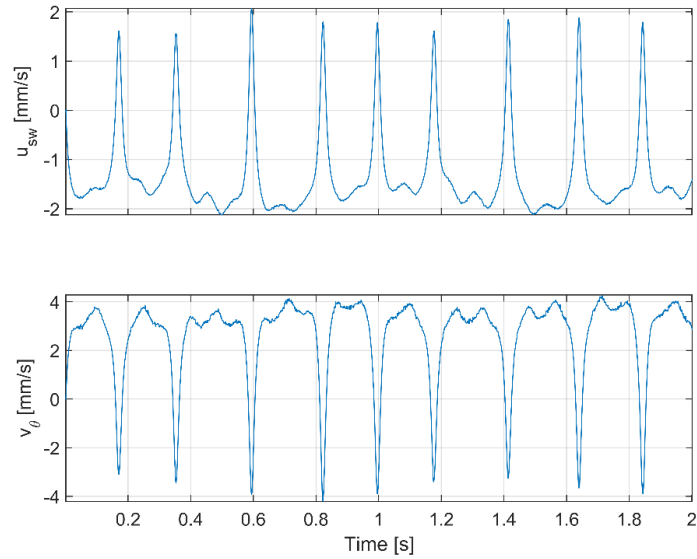
Fig. 3.16. Sudden changes in u_{sw} and v_θ as the swimmer hits the virtual channel boundaries. The data are from simulation D1.6-L4-Q0, 15 Hz. The wall force causes rotation in negative direction and a slight movement in opposite direction.

In the puller-mode, trajectories start as helices and converge to straight lines after a few rounds. Since the swimmer is larger this time, it cannot follow a helical trajectory as in Fig. 3.14. Values of u_{sw} tend to be a bit higher in simulations. As a final set of simulations in the narrow channel, D1.6-L6 experiments are carried out, with results shown in Fig. 3.17, Table 3.6 and Table 3.7. This time, the puller-mode is not simulated as similar outputs compared to previous ones are expected. Instead, cases with flow in **-x** direction are simulated. The common difference in these simulations is that β is higher than the experimental ones, as was in D1.6-L1.4 simulations. Higher the flow rate, closer the β values to experimental observations. Both u_{sw} and v_θ results in simulations are significantly larger in magnitude than experiment results. While leads were too small in D1.6-L1.4 simulations, this time lead values are mostly larger than experiments when flow is in **+x** direction (given in Table 3.6). Interestingly, when flow direction is reversed, the lead values are much closer; yet still they are higher than they are in experiments. Considering the differences observed in D1.6-L1.4, D1.6-L4 and D1.6-L6, the simulation model seems to give results most accurately for D1.6-L4 configuration while the lead and velocity values turn out lower in magnitude in D1.6-L1.4 configuration and the values are higher in D1.6-L6 configuration.

50
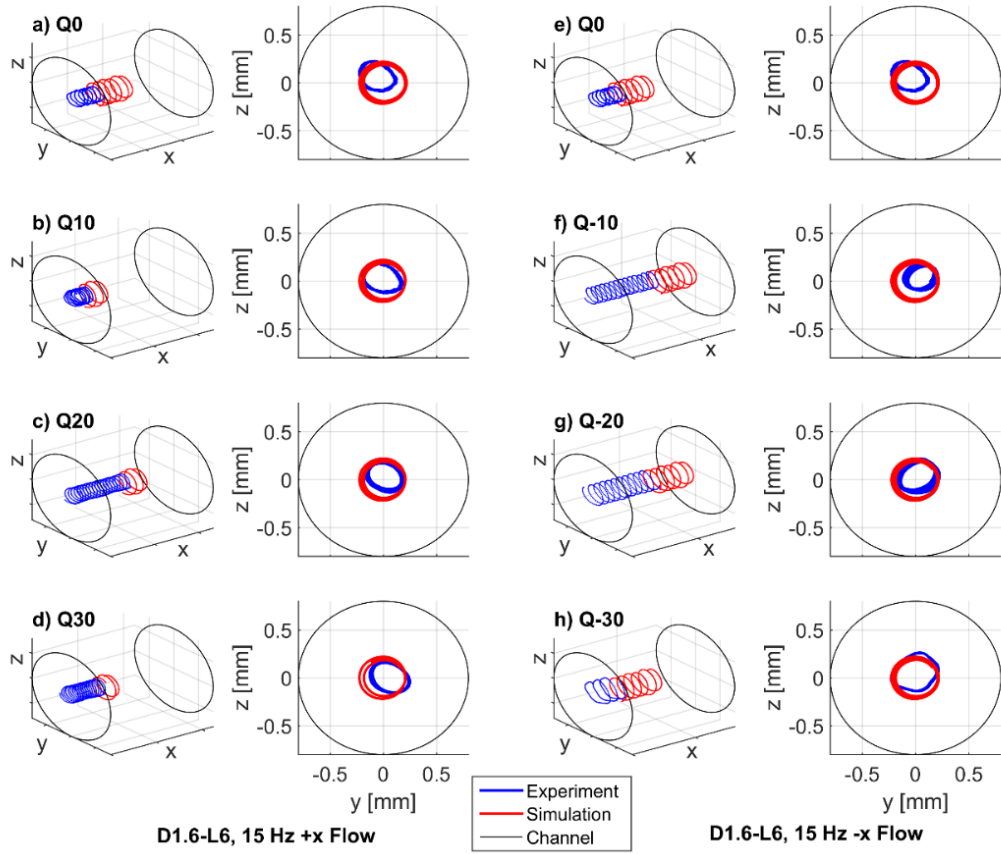
Fig. 3.17. Trajectories of simulations (in red) compared to experiment results (in blue) for D1.6-L6 configuration. a) to d) show results for flow in +**x** direction, e) to h) show for flow in -**x** direction.

Table 3.6. Comparison of lead values of D1.6-L6 experiments and simulations.

Experiment set	Lead Value (Experiment)	Lead Value (Simulation)
D1.6-L6-Q0, 15 Hz	0.552 mm	0.822 mm
D1.6-L6-Q10, 15 Hz	0.397 mm	0.727 mm
D1.6-L6-Q20, 15 Hz	0.346 mm	0.635 mm
D1.6-L6-Q30, 15 Hz	0.220 mm	0.564 mm
D1.6-L6-Q-10, 15 Hz	0.659 mm	0.930 mm
D1.6-L6-Q-20, 15 Hz	0.811 mm	1.025 mm
D1.6-L6-Q-30, 15 Hz	1.219 mm	1.120 mm

Table 3.7. Comparison of velocity values of D1.6-L6 experiments and simulations.

Experiment set	u_{sw} (Experiment)	u_{sw} (Simulation)	v_θ (Experiment)	v_θ (Simulation)
D1.6-L6-Q0, 15 Hz	-0.962 mm/s	-2.433 mm/s	0.7669 mm/s	3.86 mm/s
D1.6-L6-Q10, 15 Hz	-0.6016 mm/s	-2.154 mm/s	0.9584 mm/s	3.793 mm/s
D1.6-L6-Q20, 15 Hz	-0.887 mm/s	-1.88 mm/s	2.439 mm/s	3.791 mm/s
D1.6-L6-Q30, 15 Hz	-0.5916 mm/s	-1.597 mm/s	2.694 mm/s	3.78 mm/s
D1.6-L6-Q0, 15 Hz,	-0.962 mm/s	-2.433 mm/s	0.7669 mm/s	3.86 mm/s
D1.6-L6-Q-10, 15 Hz	-1.775 mm/s	-2.737 mm/s	2.285 mm/s	3.868 mm/s
D1.6-L6-Q-20, 15 Hz	-2.106 mm/s	-3.041 mm/s	2.738 mm/s	3.872 mm/s
D1.6-L6-Q-30, 15 Hz	-1.83 mm/s	-3.345 mm/s	1.869 mm/s	3.888 mm/s

In the wider channel, D3-L4 results are given in Fig. 3.18, Table 3.8 and Table 3.9. Note that β values are lower in simulations than in experiments at D3-L4-Q70 configuration but for other cases β values are very close. Results for u_{sw} are within the variation band of experimental observations and mostly are close to average value. Values of v_θ in simulations exhibit high variation and are significantly larger in the pusher-mode. In the puller-mode, while there is still large variation, average values are closer to experimental observations.
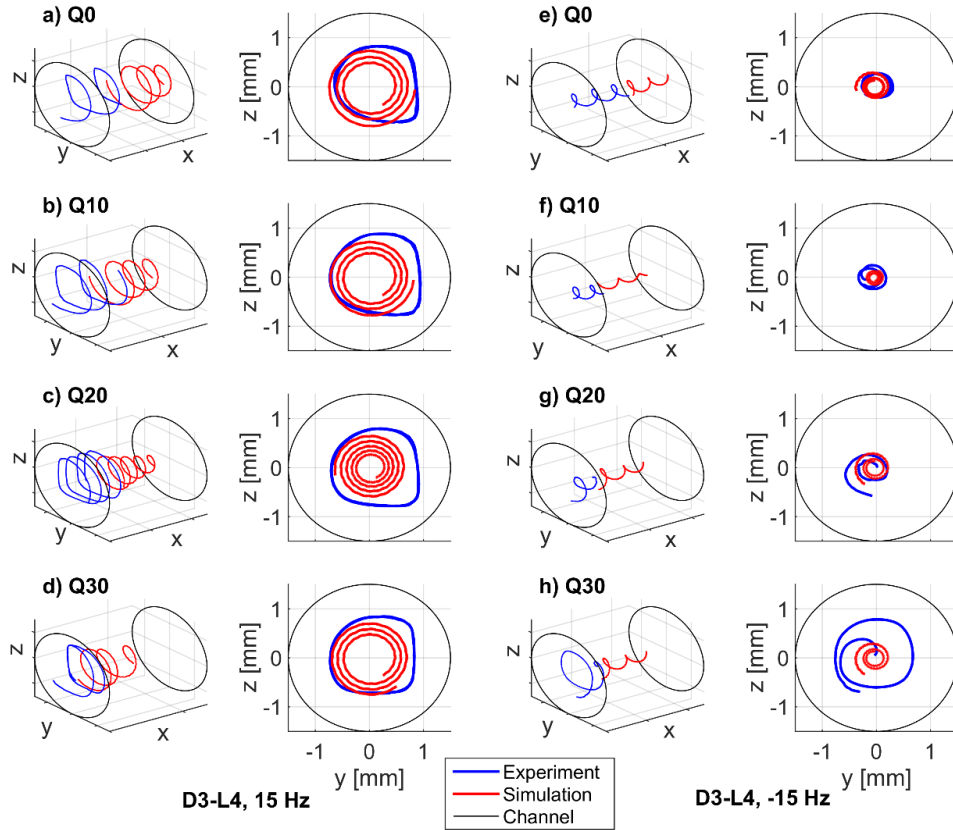
Fig. 3.18. Trajectories of simulations (in red) compared to experiment results (in blue) for D3-L4 configuration. a) to d) show pusher mode, e) to h) show puller mode.

Table 3.8. Comparison of lead values of D3-L4 experiments and simulations.

Experiment set	Lead value (Experiment)	Lead value (Simulation)
D3-L4-Q0, 15 Hz	3.8587 mm	2.092 mm
D3-L4-Q10, 15 Hz	2.1592 mm	1.685 mm
D3-L4-Q20, 15 Hz	1.3391 mm	1.389 mm
D3-L4-Q30, 15 Hz	0.013 mm	1.517 mm

Table 3.9. Comparison of velocity values of D3-L4 experiments and simulations.

Experiment set	u_{sw} (Experiment)	u_{sw} (Simulation)	v_θ (Experiment)	v_θ (Simulation)
D3-L4-Q0, 15 Hz	-1.274 mm/s	-1.511 mm/s	1.245 mm/s	3.187 mm/s
D3-L4-Q10, 15 Hz	-0.6476 mm/s	-1.204 mm/s	1.714 mm/s	3.137 mm/s
D3-L4-Q20, 15 Hz	-0.6427 mm/s	-1.01 mm/s	2.777 mm/s	2.183 mm/s
D3-L4-Q30, 15 Hz	-0.1838 mm/s	-0.8589 mm/s	1.535 mm/s	2.913 mm/s
D3-L4-Q0, -15 Hz	1.799 mm/s	2.016 mm/s	-0.8331 mm/s	-0.8069 mm/s
D3-L4-Q10, -15 Hz	1.761 mm/s	2.343 mm/s	-0.8571 mm/s	-0.4442 mm/s
D3-L4-Q20, -15 Hz	2.133 mm/s	2.94 mm/s	-1.35 mm/s	-0.8373 mm/s
D3-L4-Q30, -15 Hz	2.26 mm/s	3.135 mm/s	-1.791 mm/s	-0.8402 mm/s

4

MAGNETIC FIELD MODULATION

This chapter presents the results for experiments where the magnetic field is modulated. Modulated magnetic fields are first tested to see if the swimmer's orientation and the trajectory are affected by the modulation. By applying a sine wave in the same frequency and phase as I_1 and I_2, the swimmer can be tilted up or down in x-y plane. The swimmer is tilted in **+y** direction when $I_3=-I_1=-\sin(\omega t)$ and tilted in **-y** direction when $I_3=I_1\sin(\omega t)$. The swimmer is tilted in **+z** direction when $I_3=I_2=\cos(\omega t)$ and in **-z** direction when $I_3=-I_2=-\cos(\omega t)$. Fig. 4.1 shows the projections of 3D trajectories of swimmer L3 at the channel D3 without flow at 5 Hz with and without these modulations on y-z plane. 5 Hz is selected as rotation rate to be able to observe the effects of modulation clearly and to be able to be able to apply alternating modulation (to be discussed below) as the period of alternation cannot go very high due to limitations of experimental setup. Without any modulation, the swimmer follows a helical trajectory, as expected. When the magnetic field is modulated, tilting in the orientation of the swimmer is easily visible in experiments.

Tilting in **-y** direction decreases β significantly, with **+y** tilt resulting in a trajectory similar to that without any tilt. The difference in β is visible in the tilts in **z-** axis, although difference there is much less. Another important change with modulation is in the relative orientation of tail. Without any modulation, the tail is always pointed towards the channel wall, in line with the observations in section 3.1 Swimmer Trajectory. With modulation, the tail is nearly perfectly aligned with the magnetic field direction, especially when β is low.

Velocity in **x-** direction remains nearly the same but variation is either the same or increased when the magnetic field is tilted. When swimmer is pointed **-z** direction, both the average velocity and variation decreases in magnitude. On the other hand, variation and average velocity is high when the swimmer is tilted in +z direction. This observation is a direct result of gravitation: When swimmer head is trying to move against gravity, the tilted head causes instabilities. When the swimmer is tilted towards the ground, gravitation does not disturb the swimmer. For $I_3 = \sin(\cos(\omega t))$, the trajectory is similar to that of swimming without modulation, albeit the head is tilted in +z direction. For $I_3 = \cos(\sin(\omega t))$, the head is not tilted at all and the trajectory is as if there is no modulation. Wobbling is significantly increased. Note that even if the swimmer is tilted, the swimmer does not move in tilted direction. The reason is that the amplitude of the current that modulates the magnetic field is 1 A, which is less than the required current to obtain a magnetic field of the same magnitude as the other two pairs. The required current for that is 4 A but that value is high that it could damage the setup thus it is not tested. Yet still, as a proof-of-concept, it is shown that modulation in general can be used to modify swimmer orientation as desired.
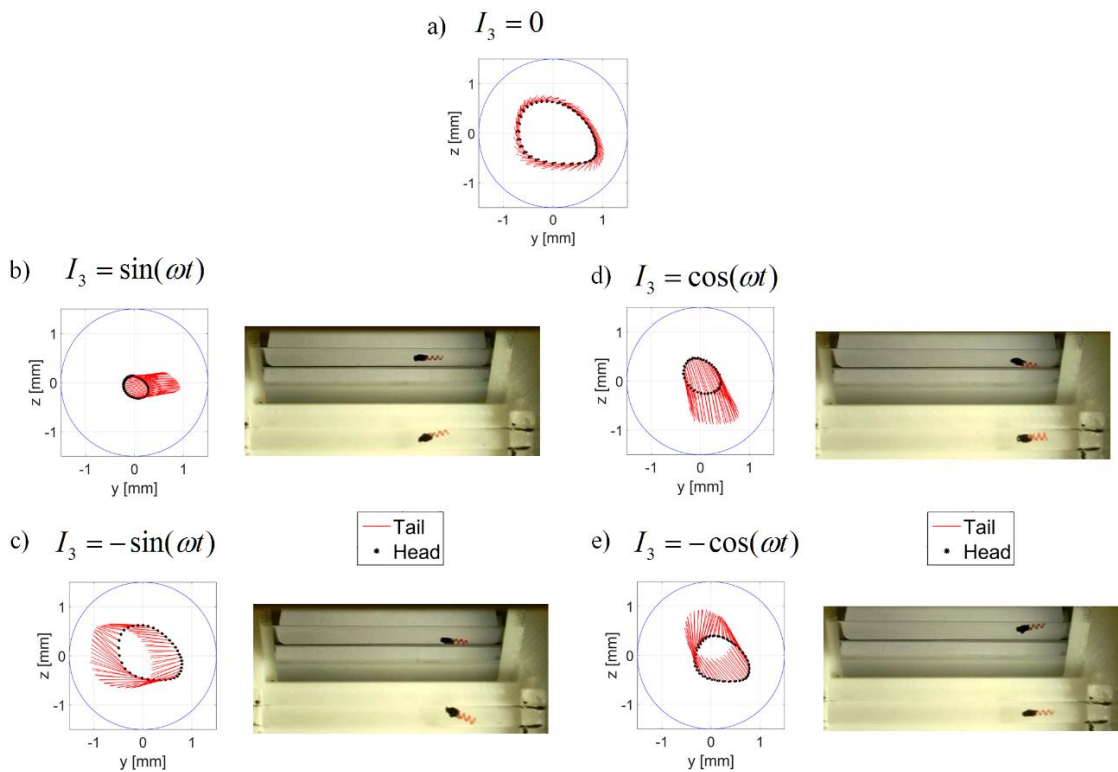
Fig. 4.1. Tilting the swimmer in one direction. a) shows swimmer trajectory when there is no modulation. b) and c) show tilting in x-y plane alongside captures from experiment recordings. d) and e) show tilting in x-z plane alongside captures from experiment recordings.

55

Several other modulations are applied. The first is doubling the frequency of the sinusoidal wave, I_3 is taken as -sin($2\omega t$). When I_3 was -sin(ωt), the swimmer was tilted in **-y** direction. As the frequency is doubled, it becomes as if there is no modulation, with the swimmer tracing out a trajectory very similar to the case when there is no modulation. For modulation to be observable, the current should have the same angular frequency as the ones sent to other coils. Next, the amplitude of the wave is increased, with the frequency reduced to its original value. As expected, it results in an increase in tilting of the swimmer in **y-** direction; however the swimmer doesn't move towards the tilted direction again. Interestingly, the increase in tilting results in the swimmer following a path very close to the centerline. Swimming velocity increases in magnitude as well. Thus, in principle it is possible for a pusher to follow a straight trajectory by significant amount of modulation in the correct direction. In other words, the orientation of the swimmer should be controllable with the modulation of the magnetic field using the coils that generate a field in the **x-** direction. The effect of the phase difference is tested with I_3=sin($\omega t+\pi/4$) and the swimmer is found to be tilted towards **-y** direction but also slightly towards **+z** direction. The major change, however, is that the swimmer follows a circular path with a very low β. Though some more complicated control mechanisms are tested as well, these last two methods prove to be very effective.
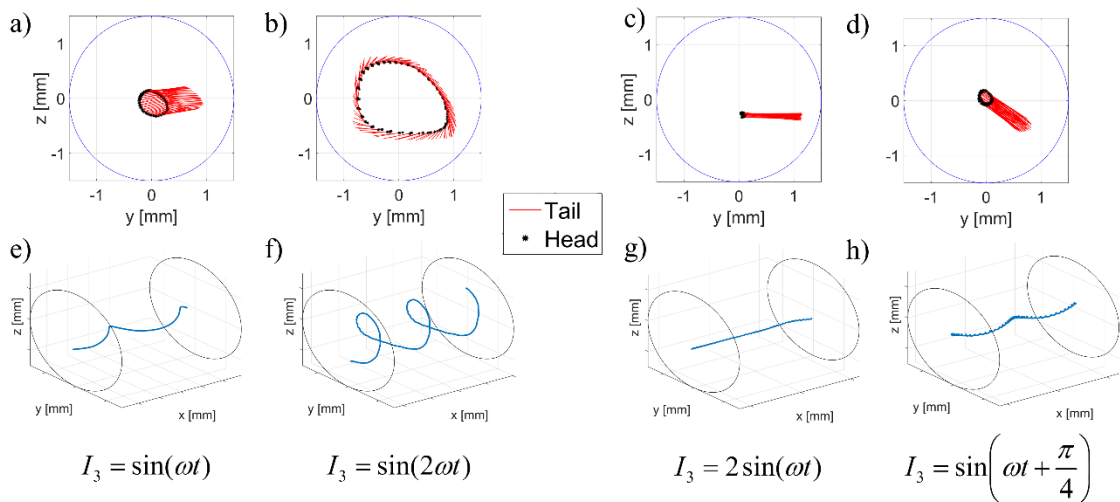
Fig. 4.2. Change in swimmer trajectory by changing parameters of the function used to tilt the swimmer in -y direction. a) to d) show projections of 3D trajectories on y-z plane and e) to f) show full 3D trajectories.

Sum of sinusoidal functions can be used to tilt the swimmer diagonally in y-z plane. When I_3 = cos(ωt)-sin(ωt), the swimmer is tilted in **+y** and **+z** directions, shown in Fig. 4.3. Note that β is once again lower compared to β without modulation. When I_3=sin($\omega t+\pi/4$), diagonal tilting was observed as well as the phase difference can be

formulated in sum of sine and cosine functions. The swimmer can be tilted in **+y** and **-z** directions with $I_3 = -\cos(\omega t) + \sin(\omega t)$,. The signs of sine and cosine functions can be altered to tilt the swimmer in desired directions; i.e., if one wishes to tilt the swimmer in **-y** and **-z** directions, $I_3 = -\sin(\omega t) + \cos(\omega t)$ will tilt the swimmer in that direction. However, these tilts contribute to swimming velocity differently as a tilt in **+z** direction decreases the velocity in magnitude and increases the variation.

$$I_3 = \cos(\omega t) - \sin(\omega t)$$
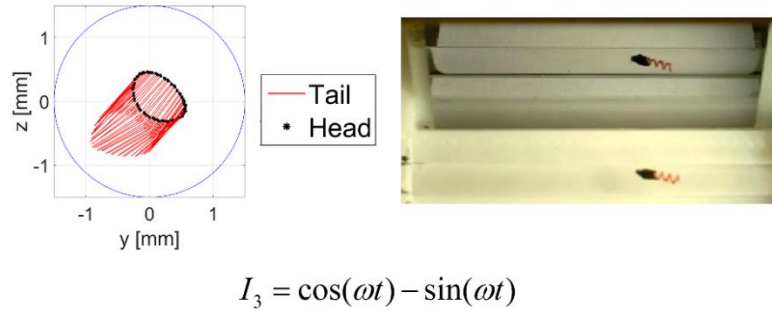
Fig. 4.3. Superposition of functions to tilt the swimmer in both x-y and x-z planes in desired directions.

Before discussing more complicated controlling attempts, it is noteworthy to highlight the effects of constant current. When constant current is given, the magnetic field is shifted in **x-** axis. Current values tested are 1, 2, -1 and -2 A. First of all, there is no difference in swimmer behavior when positive and negative current is given to the modulating coil pair. The most significant change in swimmer behavior is increased wobbling. Wobbling increases further when the magnitude of the current is increased. Increase in wobbling increases β, with the swimmer hitting channel walls. In general, swimming trajectories are similar to that of swimming without modulation. u_{sw} decreases to nearly around 0 mm/s when modulated field is shifted in **+x** direction and swimmer is far at the other end of the channel. The modulated field stops the swimmer motion without stopping the rotation of the swimmer. Effective use of modulation would allow to stop swimming without stopping rotation which could be helpful in eliminating transient behavior so that swimmer can resume its swimming in a steady fashion. This modulation can be used in mixing, pumping or abrasion on the walls as well.

Another modulation method tested is alternated modulation. As the swimmer traces out a helical trajectory, modulation direction has to be changed. For example, as the swimmer goes down in **y-** direction, modulation should be such that the swimmer should move up. The alternation mechanism is based on swimming period. Period for the

reference case is around 1 seconds, so nearly each 0.25 seconds a different kind of modulation is required. The drivers supply two different formulations of current periodically. Due to limitations of hardware, it is not possible to alternate the current in about less than 0.2 seconds. If one goes below this threshold, no modulation effect is observed. That is why the reference case is chosen at the rotation rate of 5 Hz. Though motion in x-y and x-z planes are a little out of phase, the swimmer is approximately at its maximum **y-** position when it is at its minimum **z-** position and vice versa. So, two current formulations to be supplied are:

$$I_3 = -\sin(\omega t) + \cos(\omega t) \tag{3.1}$$

$$I_3 = \sin(\omega t) - \cos(\omega t) \tag{3.2}$$

The challenge in supplying alternating current formulations is synchronizing it with the swimmer motion without any visual feedback. The initial position of the swimmer can't be fixed to ensure perfect synchronization. When the period is set to a value of 0.3 or 0.5 seconds, it is observed that above formulations combine into one, so the swimmer has a stable tilt in **-y** and **-z** directions. The trajectories are straight and close to the centerline (Fig. 4.4 a)). When angular frequency is doubled, the wobbling increases but the swimmer still follows a straight path close to the center (Compare Fig. 4.4 d) and e)).
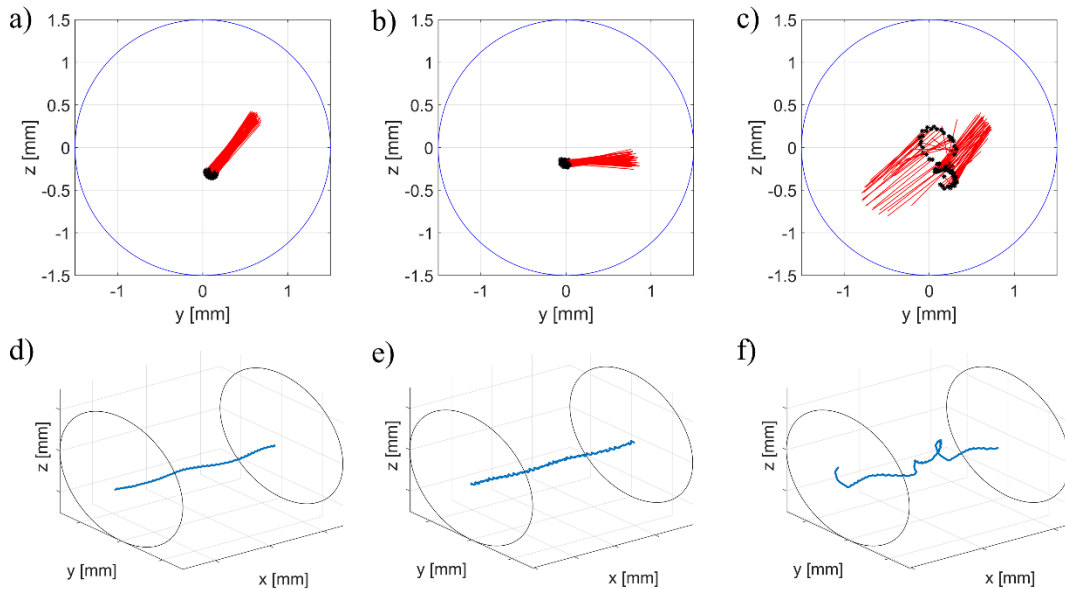
Fig. 4.4. 2D and 3D trajectories of swimmers under alternated modulation when period is 0.5 seconds (a) and d)), 0.5 seconds with twice the angular frequency (b) and e)) and 0.2 seconds (c) and f)).

Going back to alternated modulation problem, one more important point is when to apply which formulation. When the swimmer is going down in the **y-** direction, the tail should be oriented such that the tail's end is tilted in **+y** direction. The swirling flow in pusher mode pulls the swimmer towards channel walls, that's why the tail should be tilted towards the opposing wall so that the swimmer would be pulled towards the opposite channel wall. Achieving this in both x-y and x-z planes are challenging as the motion in x-y plane and x-z plane are not in phase. Fig. 4.4 c) shows an experiment that is successful to a degree; the swimmer tail is tilted in **+y** direction when head is positioned downwards in **-y** direction and tail is tilted in **-y** direction when head is positioned upwards in **+y** direction. The 3D trajectory in Fig. 4.4 f) shows that the swimmer mostly follows a straight trajectory contrary to what's observed at 2D projection figure.

5

CONCLUSION

Micro swimming robots are useful agents for various biomedical applications and micro systems. In this thesis, trajectories and velocities of magnetically actuated swimmers with helical tails are analyzed in circular channels filled with glycerol to ensure low Reynolds number swimming. The effects of magnetic field rotation rate, swimmer tail length, channel size and fluid flow are investigated. A contrast-based image processing algorithm is developed to extract 3D swimmer position and orientation. The studies are verified with time-averaged and time-dependent kinematic CFD models. Magnetic field is modulated to explore control options and swimmer behavior under different magnetic fields.

Depending on the rotation direction of the magnetic field, two swimming modes are observed: Pusher mode is when the swimmer moves in the tail direction and puller mode is when the swimmer moves in head direction. These two swimming modes differ in trajectories they trace out: Pushers follow a helical trajectory at all times while pullers follow a straight trajectory at the channel's centerline under significant confinement. The helical trajectory the pushers follow is a right-handed helix which is correlated with the swimmer's left-handed helical tail and counter-clockwise rotation. Moreover, the CFD model confirms that the lateral velocity of the swimmer is in the direction of the rotating flow. β increases at low rotation rates as the swirling flow is not able to lift up the swimmer. At high rotation rates, the magnetic torque that rotates the swimmer is not able to overcome the viscous torque, so step-out occurs which causes various instabilities such as increase in β and decrease at u_{sw}. Lateral velocity is around zero in puller mode and increases linearly with rotation rate in pusher mode up until step-out. After step-out, the decrease in lateral velocity is exponential.

The increased tail length is helpful in stabilizing the swimmer towards the centerline of the channel. Increase in tail length increases helical lead due to increased propulsion. The amount of confinement, L/D ratio is critical in the way the swimmer follows the helical trajectory: If L/D is small, both the head and the tail follow the trajectory, with the tail pointing outwards to channel walls. If L/D is large, swimmer head follows the helical path, with the tail oriented towards the centerline of the channel at all times. Increased tail length increases u_{sw} but lateral velocity is mostly unchanged.

Increase in channel size causes the swimmer to follow a helical trajectory with higher β. Pullers also start to exhibit non-straight trajectories but still not fully developed helical trajectories. With increased range of motion, variation in orientation angles, swimming and lateral velocities increase. Considering the same swimmers, increase in channel size does not cause any change in u_{sw}. The swimmer is able to swim against higher flow rates in wider channels due to a decrease in wall shear effects. On the other hand, step-out begins at smaller rotation rates.

Increased flow rate increases instability in trajectories. β is affected differently depending on L/D ratio: If L/D is small, β decreases and if L/D is large, β increases. Increased flow rate decreases helical lead significantly especially at low rotation rates. When flow is given from the tail side, average β and variation increases, signaling increased instability as the swirling flow from the tail and flow from the syringe pump are mixed. The amount of change in lead is higher when flow is given from tail side compared to head side. Flow from tail side is more effective on the swimmer. Flow suppresses step-out as the step-out rotation rate increases. This is up to a limit though: At highest flow rate, step-out rotation rate decreases. If flow is given from the tail side, the step-out rotation rate decreases, in agreement with the increased instability. Flow from both directions increase propulsion similarly but flow from tail side hinders propulsion much more. When flow is from the tail side, lateral velocity decreases significantly compared to the case when flow is in head direction. Variation is observed to increase.

The results are first verified with two CFD models: The first one is a CFD model that outputs snapshot solutions. In terms of u_{sw}, simulation results are mostly in agreement with the experiments. Since in this model it is assumed the swimmer is always in synchronization with the rotating magnetic field, simulation and experiment results diverge from each other in pusher mode as the simulations output higher velocity values.

Lateral velocity values are mostly in agreement with the experimental results, albeit they are a bit higher for the cases in the narrow channel. In the wider channel, the results diverge much more from each other.

The second CFD model, time-dependent one, takes gravitation, magnetic, fluid and wall forces into account. The model is able to replicate an experiment fully, giving out necessary position, orientation and velocity information. The model is tested under various experiment configurations for the rotation rate of 15 Hz. Transient trajectories observed in Acemoglu and Yesilyurt [24] are observed in this model as well. 3D trajectories are captured best when the tail length is 4 mm. For smaller tail length, the helical lead of the trajectory is too small while the helical lead is higher when tail length is higher than 4 mm. u_{sw} values are generally in agreement with the experiments but variations of the values are much higher. One reason for higher variation is found to be due to collision with the virtual channel walls in the simulations which cause the swimmer to slow down significantly for very small periods of time. When these spikes are excluded and average values are investigated, it is seen that the simulation results reflect the experimental observations very well. Lateral velocities, on the other hand, are generally higher in magnitude than experimental observations. Transient part of the trajectories are thought to be partially responsible for the difference as high variation is observed alongside higher values in average.

The magnetic field is modulated in several ways to explore controllability options. The swimmer can be tilted up or down with cosine function; right or left with sine function on y-z plane. Sum of these functions can be used to tilt the swimmer diagonally. Tilting the tail in +y or +z direction is effective in decreasing β. When angular frequency of the sinusoidal wave is doubled, the trajectory is similar to the case when there is no modulation and the swimmer is not tilted. When the amplitude of the sinusoidal wave is increased, the amount of tilting is increased. The increase in tilt in **-y** direction causes the swimmer to follow a path very close to the center of the channel, like a puller. Adding in phase difference leads to a helical trajectory with very small β. Constant current increases swimmer wobbling and it can be used to stop the swimmer propulsion without stopping swimmer rotation which would be helpful to eliminate transient effects. Since the swimmer in pusher mode follows a helical trajectory, it is thought that alternated modulation depending on the position of the swimmer could help in straightening the trajectory. Since there is no visual feedback and it is hard to fix initial swimmer position

and orientation, this method needs further enhancements such as visual feedback. However, for certain period values, the swimmer head is kept close to the channel center. For other period values, a non-straight trajectory could be obtained that is closer to the channel centerline than the trajectory without any modulation.

Overall, the aim of this thesis is to present an overall picture of trajectories and velocities of swimmers with helical tails. The experimental observations help us understand the underlying dynamics of low Reynolds number swimming. The CFD models are a way of validating the experimental observations. The time-dependent model enables testing many kinds of parameterizations and it is a significant step in building fully capable models that portray microswimmer motion in circular channels.

5.1. Future Work

As future work, there are two major areas: One is to improve time-dependent CFD model as there are various discrepancies in its output compared to experimental results. Magnetic, fluid, gravitational and wall forces are considered in the model but there seems to be a necessity to develop them further in order to better reflect the real-life situation. Another issue with the model is that this model prevents near-wall dynamics to be studied. While the available modelling for near-wall interactions gives results close to those of experiments, what the swimmer does in the region beyond the virtual walls remains a question.

The second area is developing a vision-based control algorithm that uses magnetic field modulation as control input. While in this thesis basic control options are explored, these options are not used to the full extent. Also, while it is shown that the swimmer can be tilted in any desired direction, the swimmer is not navigated in those directions. Experiment hardware should be modified to improve modulation capabilities. When hardware limitations are overcome, the swimmer can be made to navigate in complicated channel structures that would mimic vascular system.

6

REFERENCES

[1]   Zhang, L., Abbott, J. J., Dong, L., Kratochvil, B. E., Bell, D., & Nelson, B. J. (2009). Artificial bacterial flagella: Farication and magnetic control. *Applied Physics Letters*, 94(6), 064107.

[2]   Tottori, S., Zhang, L., Peyer, K. E., & Nelson, B. J. (2013). Assembly, disassembly, and anomalous propulsion of microscopic helices. *Nano letters*, 13(9), 4263-4268.

[3]   Martel, S. (2013). Microrobotics in the vascular network: Present status and next challenges. *Journal of Micro-Bio Robotics* 8(1), 41-52.

[4]   Purcell, E. M. (1977). Life at low Reynolds number. *American Journal of Physics*, 45(1), 3-11.

[5]   Li, G., Tam, L. K., & Tang, J. X. (2008). Amplified effect of Brownian motion in bacterial near-surface swimming. *Proceedings of the National Academy of Sciences*, 105(47), 18355-18359.

[6]   Alt, W., Hoffmann, G. (1990). Biological motion: Proceedings of a workshop held in Königswinter, Germany, March 16-19, 1989. Berlin: Springer-Verlag Berlin Heidelberg

[7]   Lauga, E. (2016). Bacterial hydrodynamics. *Annual Review of Fluid Mechanics*, 48, 105-130.

[8]   Liu, Z. & Papadopoulos, K. D. (1995). Unidirectional motility of Escherichia coli in restrictive capillaries. *Applied and environmental microbiology*, 61(10), 3567-3572

[9]   Liu, B., Gulino, M., Morse, M., Tang, J. X., Powers, T. R. & Breuer, K. S. (2014). Helical motion of the cell body enhances Caulobacter crescentus motility. *Proceedings of the National Academy of Sciences*, 111(31), 11252-11256.

[10]   Lele, P. P., Roland, T., Shrivastava, A., Chen, Y. & Berg, H. C. (2016). The flagellar motor of Caulobacter crescentus generates more torque when a cell swims backwards. *Nature Physics*, 12, 175-178.

[11]   Magariyama, Y., Sugiyama, S., Muramoto, K., Kawagishi, I., Imae, Y. & Kudo, S. (1995). Simultaneous measurement of bacterial flagellar rotation rate and swimming speed. *Biophysical Journal*, 69, 2154-2162.

[12]   Berke, A., P., Turner, L., Berg, H. C. & Lauga, E. (2008). Hydrodynamic attraction of swimming microorganisms by surfaces. *Physical Review Letters*, 101(3), 038102.

[13]   Galajda, P., Keymer, J., Chaikin, P., Austin, R. (2007). A wall of funnels concentrates swimming bacteria. Journal of Bacteriology, 189(23), 8704-8707.

[14]   Hyon Y., Marcos, Powers, T. R., Stcoker, R., Fu, H. C. (2012). The wiggling trajectories of bacteria. *Journal of Fluid Mechanics*, 705, 58-76.

[15]   Lauga, E., DiLuzio, W. R., Whitesides, G. M., & Stone, H. A. (2006). Swimming in circles: Motion of bacteria near solid boundaries. *Biophysical Journal*, 90(2), 400-412.

[16]   Biondi, S. A., Quinn, J. A., & Goldfine, H. (1998). Random motility of swimming bacteria in restricted geometries. *AIChE Journal,* 44(8), 1923-1929.

[17]   Berg, H. C., & Turner, L. (1990). Chemotaxis of bacteria in glass capillary arrays. *Biophysical Journal*, 58(4), 919-930.

[18]   DiLuzio, W. R., Turner, L., Mayer, M., Garstecki, P., Weibel, D. B., Berg, H. C., & Whitesides, G. M. (2005). Escherichia coli swim on the right-hand side. *Nature*, 435(7046), 1271-1274.

[19]   Männik, J., Driessen, R., Galajda, P., Keymer, J. E., & Dekker, C. (2009). Bacterial growth and motility in sub-micron constrictions. *Proceedings of the National Academy of Sciences*, 106(35), 14861-14866.

[20]   Honda, T., Arai, K. I., & Ishiyama, K. (1996). Micro swimming mechanisms propelled by external magnetic fields. *Magnetics, IEEE Transactions on,* 32(5), 5085-5087.

[21]   Dreyfus, R., Baudry, J., Roper, M. L., Fermigier, M., Stone, H. A., & Bibette, J. (2005). Microscopic artificial swimmers. *Nature*, 437(7060), 862-865.

[22]   Ghosh, A., & Fischer, P. (2009). Controlled propulsion of artificial magnetic nanostructured propellers. *Nano letters*, 9(6), 2243-2245.

[23]   Palagi, S., Mark, A. G., Reigh, S. Y., Melde, K., Qiu, T., Zeng, H., Parmeggiani, C., Martella, D., Sanchez-Castillo, A., Kapernaum, N., Giesselmann, F., Wiersma, D. S., Lauga, E., & Fischer, P. (2016). Structured light enables biomimetic swimming and versatile locomotion of photoresponsive soft microrobots. *Nature Materials*, 15, 647-654.

[24]   Acemoglu, A., & Yesilyurt, S. (2015). Effects of Poiseuille flows on swimming of magnetic helical robots in circular channels. *Microfluidics and Nanofluidics*, 19(5), 1109-1122.

[25]   Abbott, J. J., Lagomarsino, M. C., Zhang, L., Dong, L., & Nelson, B. J. (2009). How should microrobots swim? *The International Journal of Robotics Research*.

[26]   Liu, B., Powers, T. R., Breuer, K. S. (2011). Force-free swimming of a model helical flagellum in viscoelastic fluids. *Proceedings of the National Academy of Sciences*, 108(49), 19516-19520.

[27]   Man, Y., & Lauga, E. (2013). The wobbling-to-swimming transition of rotated helices. *Physics of Fluids*, 25(7), 071904.

[28]   Johnson, R. E., & Brokaw, C. J. (1979). Flagellar hydrodynamics: A comparison between resistive-force theory and slender-body theory. *Biophysical Journal*, 25, 113-127.

[29]   Felderhof, B. U. (2010). Swimming at low Reynolds number of a cylindrical body in a circular tube. *Physics of Fluids*, 22(11), 113604.

[30]   Ligthill, J. (1976). Flagellar hydrodynamics. *SIAM review*, 18(2), 161-230.

[31]   Phan-Thien, N., Tran-Cong, T., & Ramia, M. (1987). A boundary-element analysis of flagellar propulsion. *Journal of Fluid Mechanics*, 184, 533-549.

[32]   Shum, H., Gaffney, E. A., & Smith, D. J. (2010). Modelling bacterial behaviour close to a no-slip plane boundary: the influence of bacterial geometry. *Proceedings of the Royal Society*, 466, 1725-1748.

[33]   Shum, H., & Gaffney, E. A. (2015). Hydrodynamic analysis of flagellated bacteria swimming in corners of rectangular channels. *Physical Review E.*, 92, 036016.

[34]   Goto, T., Masuda, S., Terada, K. & Takano, Y. (2001). Comparison between observation and boundary element analysis of bacterium swimming motion. *JSME International Journal Series C*, 44(4), 958-963.

[35]   Zöttl, A., & Stark, H. (2012). Nonlinear dynamics of a microswimmer in Poiseuille flow. *Physical Review Letters*, 108(32), 218104.

[36]   Zöttl, A., & Stark, H. (2013). Periodic and quasiperiodic motion of an elongated microswimmer in Poiseuille flow. *The European Physical Journal E,* 36(4), doi: 10.1140/epje/i2013-13004-5.

[37]   Graaf de, J., Mathijssen, A. J. T. M., Fabritius, M., Menke, H., Holm, C., & Shendruk, T. N. (2016). Understanding the onset of oscillatory swimming in microchannels. *Soft Matter*, 12, 4704-4708.

[38]   Chacón, R. (2013). Chaotic dynamics of a microswimmer in Poiseuille flow. *Physical Review E*, 88(5), 052905.

[39]   Zhu, L., Lauga, E., & Brandt, L. (2013). Low-Reynolds-number swimming in a capillary tube. *Journal of Fluid Mechanics*, 726, 285-311.

[40]   Keaveny, E. E., & Maxey, M. R. (2008). Spiral swimming of an artificial micro-swimmer. *Journal of Fluid Mechanics*, 598, 293-319.

[41]   Temel, F. Z., & Yesilyurt, S. (2013). Simulation-based analysis of micro-robots swimming at the center and near wall of circular mini-channels. *Microfluidics and Nanofluidics*, 14(1-2), 287-298.

[42]   Zhang, L., Abbott, J. J., Dong, L., Kratochvil, B. E., Bell, D., Nelson, B. J. (2009). Artificial bacterial flagella: Fabrication and magnetic control. *Applied Physics Letters*, 94, 064107.

[43]   Nourmohammadi, H., Keighobadi, J., Bahrami, M. (2016). Design, dynamic modelling and control of a bio-inspired helical swimming microrobot with three-dimensional manoeuvring. *Transactions of the Institute of Measurement and Control*, doi: 10.1177/0142331215627006

[44]   Oulmas, A., Andreff, N., Régnier, S. (2016). Closed-loop 3D path following of scaled-up helical microswimmers. *Robotics and Automation, 2016 IEEE International Conference on*, 978-1-4673-8026-3/16.

[45]   e-Magnets UK (n.d.). Grades of neodymium. Retrieved online from http://www.ndfeb-info.com/neodymium_grades.aspx

[46]   Acemoglu, A. (2015). Effects of geometric parameters and flow on microswimmer motion in circular channels (Unpublished master's thesis). Sabanci University, Istanbul, Turkey.

[47]   MathWorks. (2014). Image Processing Toolbox: User's Guide (R2014a).

[48]   Castrejón-Pita, J. R., Hoath, S. D., & Hutchings, I. M. (2012). Velocity profiles in a cylin-drical liquit jet by reconstructed velocimetry. Journal of Fluids Engineering, 134, 011201.

[49]   COMSOL AB (2015). Comsol Mulyiphysics 5.2.: CFD Module's User Guide.

[50]   Temel, F. Z., & Yesilyurt, S. (2011, April). Magnetically actuated micro swimming of bio-inspired robots in mini channels. In Mechatronics (ICM), 2011 IEEE International Conference on (pp. 342-347). IEEE.

APPENDIX: IMAGE PROCESSING CODE

Swimmer position and orientation data are extracted from the videos using the code below. There are six inputs to the function: *rectxy* and *rectxz* are the channel boundaries in the experiment recording for x-y plane and x-z plane images. *upl* is the length of unit pixel in millimeters. *mainl* is the name of the experiment video. *orlimitxy* and *orlimitxz* are black-and-white thresholds for x-y and x-z plane images. The code loads the full video, processes each frame sequentially. First, the frames are cropped to obtain x-y or x-z plane image. Next, grayscale images are obtained and from there black-and-white binary images are obtained based on the threshold value. The centroid and orientation of the swimmer are found from these binary images. Full details can be found at section 2.2, Image Processing of Experiment Videos.

```
% This function loads respective experiment video, crops it, applies image
processing and extracts swimmer position and orientation.
% Note the original function is longer, extracting data from x-y and x-z
planes for two videos with opposing rotation rates (1 and -1 for example)
% Here only extraction from x-y plane image for one video is presented.
%
%% --- INPUTS TO THE FUNCTION --- %%
% rectxy = [xmin ymin width height] --> Channel boundaries of x-y plane image
of the swimmer, in pixels
% rectxz = [xmin ymin width height] --> Channel boundaries of x-z olane image
of the swimmer, in pixels
% upl --> unit pixel length in mm (double)
% mainl --> name of experiment video to be processed (integer)
% orlimitxy --> Binary image threshold to extract tail profile from x-y plane
image
% orlimitxz --> Binary image threshold to extract tail profile from x-z plane
image
%%
%
%% --- OUTPUTS OF THE FUNCTION --- %%
% Not available.
%%

function [] = getxy(rectxy, rectxz, upl, mainl, orlimitxy, orlimitxz)

clearvars -except mainl rectxy rectxz upl orlimitxy orlimitxz; %clear
everything except the inputs.
READ = 1; % READ = 1 if you want to read file
```

```matlab
fpref = ['D:/Vision2/Mayis/D3-L4-Q70/' num2str(mainl)]  % name of the
directory & the file prefix, note that experiment set name has to be changed
manually
if READ
    swimmerObj = VideoReader(strcat(fpref,'.mp4')); % Video name
    frames = read(swimmerObj);   %Read video and save the frames in variable
"frames"
end

OUT = 0;     % OUT = 1 if one desires to display data extraction process, as
in Fig. 2.3.

if OUT
    out = VideoWriter('test.avi'); %prepere data extraction process video
file
    open(out);
end

k1 = 1;  % Starting frame
a=size(frames);
k2 = a(4); % Ending frame

rect = rectxy; % The channel boundaries
H = rect(4); % Height of the channel in pixels

X1 = 5; %Parameters that define the search region around the swimmer body
X2 = 30;
Y1 = 10;
Y2 = 3;

orlimit = orlimitxy; % Image black & white limit to extract tail profile
poslimit = 0.05; % Image black & white limit to detect the position of the
head

WRITE = 1;  %Boolean to write extracted position and orientation data as .dat
file

if k1==k2; WRITE = 0; end %If one frame is checked, do not save extracted
data

fref = imcrop(frames(:,:,:,k1),rect); % Cropping the reference (first) frame
fref1 = rgb2gray(fref); % Black & white version of reference frame
fref2 = imadjust(fref1); % Increase contrast
figure(1)
clf
clear cent cent2 theta dir xsw ysw
xsw = zeros(k2-k1,1); % Space allocation for x-, y- (or z-) position and
orientation data
ysw = zeros(k2-k1,1);
theta = zeros(k2-k1,1);
dir =  zeros(k2-k1,1);

j = 0; % Loop counter

for k = k1:k2
    a = imcrop(frames(:,:,:,k),rect); % Crop the image down to channel
boundaries
    subplot(411);imshow(a); % Place the cropped image onto top of figure
    b1 = rgb2gray(a); % Obtain grayscale image
```

```matlab
    b2 = imadjust(b1); % Increase contrast
    b5 = imhistmatch(b2,fref2); % Histogram matching to reference frame
    subplot(412);imshow(b5) % Display the modified image
    c = im2bw(b2,orlimit);  % Image to use for orientation extraction
    c2 = im2bw(b2,poslimit);  % Image to use for position extraction
    subplot(413);imshow(c); % Show the black and white image for orientation
extraction
    j = j+1; % Increase loop counter by one

    if rect == rectxy % If x-y plane is being extracted
        cc = flipud(~c);
        cc2 = flipud(~c2); % Flip "not" of the images in transformation from
image coordinate system to Cartesian
    elseif rect == rectxz
        cc = ~c;
        cc2 = ~c2; % Take not of the images only. In first experiment group,
the image is flipped upside down so flipping once again is not required.
    else
        disp(['rectangle is not specified!!']);
    end

    s = regionprops(cc,'Centroid','Orientation','FilledArea'); % Find the
centroid, orientation and total filled area of black and white image
    s2 = regionprops(cc2,'Centroid','FilledArea'); % Find the centroid and
total filled area of black and white image
    [famax,kmax] = max(cell2mat({s.FilledArea})); % Find the largest area,
which should be the head
    cents = cell2mat({s.Centroid}); % Find the center of that area
    cent(j,:) = cents(2*kmax-1:2*kmax); % Record the position values
    cents2 = cell2mat({s2.Centroid}); % Find the centroid from the other
image as well
    [famax2,kmax2] = max(cell2mat({s2.FilledArea}));
    cent2(j,:) = cents2(2*kmax2-1:2*kmax2);

    [ii,jj,ss] = find(cc); %Collect the points
    [m,n] = size(cc);
    jsw = find(jj > cent2(j,1)-X1 & jj < cent2(j,1)+X2 & ...  % Mask the
region where the swimmer is
        ii < cent2(j,2)+Y2 & ii > cent2(j,2)-Y1 ); % approximately
    p = polyfit(jj(jsw),ii(jsw),1); % Fit a line to the points


    if p(1) > 0 % Bounding box is modified to find the tail pixels for
extreme tilts
        Y2b = Y2+p(1)*X2; Y1b = Y1;
    else
        Y1b = Y1-p(1)*X2; Y2b = Y2;
    end

    clear jsw p

    jsw = find(jj > cent2(j,1)-X1 & jj < cent2(j,1)+X2 & ...
        ii < cent2(j,2)+Y2b & ii > cent2(j,2)-Y1b ); % Mask the region where
the swimmer is approximately (recalculation)
    p = polyfit(jj(jsw),ii(jsw),1);

    theta(j) = atan(p(1));  % Find orientation angle (either theta_xy or
theta_xz)
    subplot(414)
```

```matlab
        iic = ii(jsw);

    plot([0 rect(3)+1 rect(3)+1 0 0],[0 0 rect(4)+1 rect(4)+1 0],'k-',... %
Plot the data extraction process
        jj(jsw),iic,'.',...

jj(jsw),p(2)+jj(jsw)*p(1),cent(j,1),cent(j,2),'o',cent2(j,1),cent2(j,2),'*');
    axis('equal')

    dir(j) = p(1); % Slope of the fit line

    if OUT; %If output video is to be recorded, add the figure
        frm = getframe(gcf);
        writeVideo(out,frm);
    end
end

if OUT; close(out); end % Close data extraction video

xsw = cent2(:,1)*upl; % Transformation from pixel coordinates to Cartesian
ysw = (cent2(:,2)-(H+1)/2)*upl; % y- axis is along the center of the bounding
box, define Cartesian coordinates accordingly
thdg = theta*180/pi; % Orientation angle in degrees

if (k2>k1)
    figure(3); %Plot extracted data
    subplot(211);
    plot(xsw,ysw,'.');axis('equal');xlabel('xsw [mm]'); ylabel('{ysw,zsw}
[mm]');
    subplot(212)
    plot(theta,'.');xlabel('index'); ylabel('orientation angle [deg]')
    tmp= [xsw';ysw';thdg';dir']';
    if rect == rectxy & WRITE %Record extracted data
        save(strcat(fpref,'xy.dat'),'tmp','-ascii');
    elseif rect == rectxz & WRITE
        save(strcat(fpref,'xz.dat'),'tmp','-ascii');
    end
end

end
```